CFD Benchmark Tests for Indoor Environmental Problems: Part 1 Isothermal/Non-Isothermal Flow in 2D and 3D Room Model

Kazuhide Ito*, Kiao Inthavong, Takashi Kurabuchi, Toshikatsu Ueda, Tomoyuki Endo, Toshiaki Omori, Hiroki Ono, Shinsuke Kato, Koji Sakai, Yoshihide Suwa, Hiroshi Matsumoto, Hajime Yoshino, Weirong Zhang and Jiyuan Tu

Interdisciplinary Graduate School of Engineering Science, Kyushu University, 6-1 Kasuga-koen, Kasuga, Fukuoka, 816-8580 Japan

Abstract: Commercially available Computational Fluid Dynamics (CFD) software have been applied in indoor environmental design in recent years, but the prediction accuracy depends on an understanding of fluid dynamics fundamentals, in setting appropriate boundary and numerical conditions. This study aims to provide practical modelling information related to prediction accuracy and problematic areas in CFD applications in air conditioning and ventilation, through a series of benchmark tests and reported the results. Six commercial CFD codes were evaluated while two benchmark test cases were performed on isothermal/non-isothermal flow in 2D and 3D room models. The influence of mesh design, and turbulence models showed that using a standard k-ε model on a coarse mesh could provide sufficiently accurate results for practical purposes, by reducing the relaxation coefficient. Evaluation using different CFD programs on a non-isothermal room airflow showed different performances in predicting temperature distributions. The OpenFOAM code showed the closest matching results between three codes tests.

Keywords: Indoor environment, Computational Fluid Dynamics, Benchmark test, Isothermal flow, non-isothermal flow.

1. INTRODUCTION

Indoor air flow produces a rich variety of fluid dynamics such as flow separation, recirculation, and reattachment. The accurate prediction of such behavior plays an important role in the design of ventilation systems for occupant comfort and indoor air quality [1-3]. Computational Fluid Dynamics (CFD) is a promising tool with modern CFD software now providing easy-to-use graphical user interface. However this doesn't guarantee accurate results because of the large number of variables and model settings involved.

Since Nielsen [4] applied CFD for room airflow predictions, its use for research has been prominent evident by The International Energy Agency Annex 20 project which looked at room airflow predictions with researchers from 13 countries [5], the number of indoor building related CFD papers tripling over the period between 1985 and 2003 [6], and more recently the publication of REHVA Guidebook No. 10, "Computational Fluid Dynamics in Ventilation Design" [7]. Research articles in the literature provide up to date results which can provide modelling guideline requirements for specific indoor air scenarios. Typically this is in the form of CFD setup guidelines or turbulence model selection.

*Address correspondence to this author at the Interdisciplinary Graduate School of Engineering Science, Kyushu University, 6-1 Kasuga-koen, Kasuga, Fukuoka, 816-8580 Japan; Tel: +81 92 583 7628; Fax: +81 92 583 7627; Email: ito@kyudai.jp

In terms of CFD setup guidelines, the early work by Chen [8] discussed the challenges involved in modelling HVAC citing turbulence as a major hurdle. The AIAA (American Institute of Aeronautics and Astronautics) provided a general guideline for the verification and validation of CFD simulations [9], and a later report was published by Stern *et al*. [10] for quantifying numerical (verification) and modelling (validation) errors and uncertainties. Guidelines specific to indoor air environments was presented by Sorensen and Nielsen [11], which provided recommendations for improving the quality of CFD calculations as well as reporting guidelines to allow scientific judgment of the quality of the study.

In terms of turbulence model selection, Chung [12] used the standard linear k–ε model to simulate flow in a partitioned enclosed room and showed that the model results of temperature and velocity fields agreed well with measured data. Other studies found that the RNG-k-ε variant displayed satisfactory agreement with experimental data [13-17]. Chen [18] evaluated five k-ε models including the standard and RNG model for predicting natural and forced convection flows, and found that the RNG k-ε model is slightly better than the standard k-ε model and is therefore recommended for indoor air flow simulations. The better performance of the RNG k-ε model over the standard k-ε model was also confirmed by Rouaud and Havet [19] and Gebremedhin and Wu [20], based on simulations on different geometries.

E-ISSN: 2409-9821/15

Other numerical investigations of two-dimensional room airflows [21-23] showed that isotropic turbulence models (e.g., k-ε, k-ω) were sufficient in predicting room airflows. However, this approach fails in the prediction of turbulence driven secondary motions in three-dimensional spreading diffuser jets [24-26]. For room airflows, this scenario can be observed at air diffusers or inlets that are mounted near a wall so that a three-dimensional wall jet is encountered, and improved non-linear models were suggested by Heschl *et al*. [27].

Given the large number of turbulence model choices, Nielsen [28] provides a guide for its selection to predict room airflow, published in 1998. More recently Zhang *et al*. [29] used ANSYS-Fluent to evaluate eight turbulence models ranging from the zero-equation, RANS, RSM, and LES based models on natural convection in a tall cavity, forced convection in a room with partitions, mixed convection in a square cavity, and strong natural convection in a model fire room. These reported papers contain limited number of realistic examples, their objects of analysis involved only basic and relatively simple indoor flow fields, and the simulations were limited to a single computational software.

The objective of this study is to compile CFD techniques that influence prediction accuracy and to identify problematic areas in indoor environments, air conditioning and ventilation, by performing benchmark tests. From the literature typical flow fields in indoor environments, as they relate to air conditioning and ventilation can be classified into the following eight categories:

(1) Isothermal 2-D/3-D airflows

(2) Non-isothermal 2-D/3-D airflows

(3) Cross-ventilation airflows

(4) Floor heating (panel) systems

(5) Numerical thermal manikins

(6) Air-conditioning airflows

(7) Residential kitchen airflows

(8) Fire-induced flow

For each category, benchmark experimental data are provided as validation data for the CFD simulations, of which several different commercial CFD codes were used. The benchmark test results within this paper include (1) isothermal 2-D/3-D airflows and (2) non-isothermal 2-D/3-D airflows were reported.

2. METHOD

2.1. Benchmark Testing for Isothermal Indoor Airflow Problems

The benchmark testing is driven by two themes. This includes (i) situations in which different CFD software are used, and (ii) situations in which detailed and reliable experimental data are available for mean flow and turbulence statistics related to isothermal indoor air flow. In addition, we identify precautions that should be taken when using commercially available CFD software.

In this study (Part 1), six commercial CFD codes were evaluated while two benchmark test cases (two-dimensional room Ito *et al*. [30]; and two-dimensional model room by IEA ANNEX 20 (1993) [31]) were used for isothermal model room (chamber).

2.2. Commercial CFD Code

Various commercially CFD software exist which ranging from basic industry needs to high level research. Among the CFD codes, which allow users to select turbulence models, and to some extent, the numerical setup and boundary conditions, we evaluate the following in conducting the benchmark tests.

Table 1: List of Commercial Software Evaluated in the Benchmark Testing

SOFTWARE	ABBREVIATION	
ANSYS – Fluent	FLUENT	(Code A)
ANSYS – CFX	CFX	(Code B)
CRADLE – Stream	STREAM	(Code C)
IDAJ – Star CD	Star-CD	(Code D)
OpenFOAM	OpenFOAM	(Code G)
Advanced Knowledge Laboratory – FlowDesigner	FlowDesigner	(Code H)

2.3. Turbulence Models

Due to the lower computational effort most airflow simulations are based on the Reynolds Averaged Navier Stokes (RANS) equations with a first-order-closure turbulence model using a linear correlation between the Reynolds stress tensor and the strain rate tensor (i.e. the Boussinesq approach). The RANS models have are a representative example of models that have been successfully applied in analyses of indoor turbulence fields [18,32]. Since the development of the standard *k*–ε model by Launder and Spalding [33], many variants have been developed and applied to indoor airflow analyses. Here, we introduce four turbulence models that are used in the benchmark tests.

2.3.1. Standard k–ε Model (SKE)

This fundamental model was developed for handling fully turbulent flow fields. It applies wall-surface boundary conditions using wall function assumptions to the near wall region without directly solving the region. It is widely used and has provided sufficient accuracy in analyzing cases involving simple flow fields. However, problems have been found regarding the overestimation of *k* in the impinging region, and its approximation of a linear eddy viscosity/diffusivity.

2.3.2. Low-Re k–ε Model (LRKE)

In contrast to the standard *k*–*ε* model, the Low-Re *k*–*ε* model was designed to account for damping and echo effects in the near wall region; it is also applied to quasi-laminarized flow fields existing within stable stratifications. The model implements damping and model functions, and performs low-Reynolds number corrections for the production and dissipation terms of the eddy viscosity μ_t and ε equations. The low-Re k–ε model can reproduce turbulence phenomena found around walls that result from trying to solve adequately refined mesh partitions under no-slip conditions in the region around the wall. The analyses performed in this study use the Abe-Kondoh-Nagano model [34].

2.3.3. RNG k–ε model (RNG)

This model applies the Renormalization Group (RNG) theory developed by Yakhot and Orszag [35] and is similar to the standard *k*–*ε* model (although numerical constants such as C_μ and $C_{\varepsilon 1}$ differ). It has a built-in low-Reynolds number effect that is used to calculate Prandtl numbers found in diffusion terms of transport equations for *k* and *ε* in regions with high Reynolds numbers. This occurs in the appearance of additive terms that reproduce distortion effects found in the *ε* transport equations.

2.3.4. k–ω model (KW)

This model was developed by Wilcox [36]. Here, the quantity $\omega = \varepsilon/k$ is the local (regional) scale vorticity. There is no need to use damping functions in viscous sublayers because low-Reynolds number corrections have been carried out in the coefficient of eddy viscosity μ_t. In addition, the *k*–*ω* model has been adopted for boundary layers around wall surfaces, whereas the hybrid SST *k*–*ω* model, developed by Menter [37], uses the standard *k*–*ε* model outside of boundary layers.

2.3.4. Other Models

Other turbulence models used in general-purpose CFD codes include the LK (Launder-Kato) model, the realizable *k*–*ε* model, and the nonlinear *k*–*ε* model. Although we have found analysis cases that used the

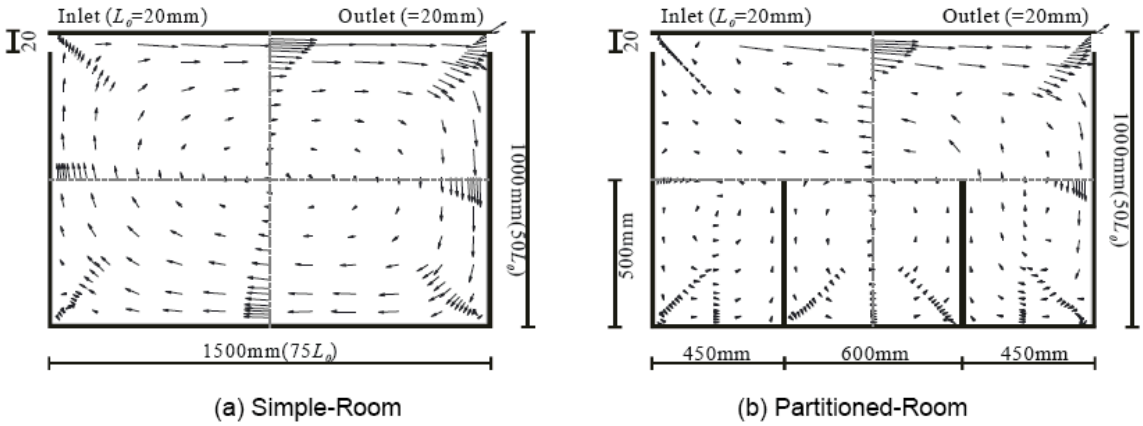

Figure 1: Schematic of the 2D room with averaged velocity vectors using LDV (Ito *et al.* 2000). (a) Simple-Room setup using a slot-type supply inlet at the top left corner, and an exhaust at the top right corner. (b) Partitioned-Room with the same inlet and exhaust and two partitions dividing the bottom half of the room into three regions.

LES model and the Detached Eddy Simulation (DES) model (a hybrid of the LES and RANS models), we did not include them in the benchmark testing described in this study because of its high computational cost.

3. RESULTS: 2D ISOTHERMAL ROOM

3.1. Benchmark Test Against Ito *et al*. [30]

Detailed measurements of an isothermal flow field in a 2D room model (1.5 m × 1.0 m) were performed using laser Doppler velocimetry (LDV). Figure **1** shows a schematic of the two scenarios that were performed: (a) a simple ventilation which used a slot-type supply inlet (L_0 = 0.02 m) along the ceiling surface and an exhaust slot-type outlet situated on the opposing wall, and (b) a partitioned room where the room was divided into occupied regions at X = 0.45 m, 1.05 m with height of Y = 0.5 m. The inlet supply was set to 3.0 m/s, and the turbulent intensity was 1.2%.

The benchmark tests investigated the influence of mesh, and turbulence model in the CFD codes FLUENT, CFX, STREAM, and Star-CD. The cases analyzed are summarized in Table **2**, and the numerical and boundary conditions in Table **3**. Mesh influence was evaluated for four structured and one unstructured mesh. Meshes A and B were coarse meshes with the first cell touching the wall surface having a y^+ of approximately 30. For Mesh A, the inlet opening contained five cells positioned at equal intervals; the remaining domain was generated with an enlargement ratio of 1.10. For Mesh B, the entire region (including the inlet) was divided into equal intervals of 10 mm. Mesh C was of moderate size (about 100,000 cells) with y^+ approximately equal to 1 (0.1 mm) for the entire field, and the mesh was generated using an enlargement ratio of 1.10. Mesh D also had with y^+ approximately equal to 1 but used enlargement ratio of 1.05 (approximately 300,000 cells). Mesh E was an unstructured mesh with approximately 200,000 cells. The mesh design for the area around the supply inlet for Meshes A–E is shown in Figure **2**.

We compared five turbulence models: (1) the standard k–ε model (*SKE*), (2) the low-Re k–ε model Abe–Kondoh–Nagano model (*LRKE*), (3) the RNG k–ε model (*RNG*), (4) the standard k–ω model (*KW*), and (5) the SST k–ω model (*SST*). To avoid truncation

Table 2: Analysis Case List

Case Name	CFD Code	Room model	Mesh	Turbulence model	Computational Algorithm
A-A-A-1	FLUENT (Code A)	Simple	Mesh A	SKE	SIMPLE Steady Algorithm
A-A-B-1			Mesh B	SKE	
A-A-C-1			Mesh C	SKE	
A-A-D-1			Mesh D	SKE	
A-A-D-2				LRKE	
A-A-D-3				RNG	
A-A-D-4				KW	
A-A-D-5				SST	
A-A-E-1			Mesh E	SKE	
A-B-D-1		Partitioned (Obstructions present)	Mesh D	SKE	
A-B-D-2				LRKE	
A-B-D-3				RNG	
A-B-D-4				KW	
A-B-D-5				SST	
B-A-D-1	CFX (Code B)	Simple	Mesh D	SKE	
B-A-D-2				SST	
B-B-D-1		Partitioned	Mesh D	SKE	
B-B-D-2				SST	
C-A-D-1	STREAM (Code C)	Simple	Mesh D	SKE	
C-A-D-2				LRKE	
C-B-D-1		Partitioned	Mesh D	SKE	
C-B-D-2				LRKE	
D-A-D-1	Star-CD (Code D)	Simple	Mesh D	SKE	
D-A-D-2				LRKE	

SKE = standard-k–ε; LRKE = low-Re-k–ε; RNG = RNG-k–ε; KW =standard-k–ω; SST = SST-k-ω.

Table 3: Boundary and Numerical Conditions

Analysis	2-Dimensional space shown in Figure **1**
Meshing	Mesh A: 94(X)×64(Y) 6, 016 cells, minimum cell width 4 mm Mesh B: 150(X)×100(Y) 15, 000 cells, minimum cell width 10 mm Mesh C: 348(X)×284(Y) 98, 832 cells, minimum cell width 0.1 mm Mesh D: 614(X)×474(Y) 291, 036 cells, minimum cell width 0.1 mm (for both cases) Mesh E: 212, 372 cells
Difference Scheme	Used QUICK for advective terms for all transport equations
Algorithm	SIMPLE
Inflow Boundaries	U_{in}=3m/s $k_{in}=3/2\cdot(U_{in}\times 0.012)^2$ $\varepsilon_{in}=C_\mu\cdot k_{in}^{3/2}/l_{in}$, $l_{in}=1/7\cdot L_0$ (The supply airflow conditions matched that found in the experiment results)
Outflow Boundaries	All of the transport variables had a gradient of zero
Wall Surface Conditions	Solid Wall, No-slip conditions for all of the cases analyzed
Other	The default values set within the CFD codes were used for all other boundary conditions.

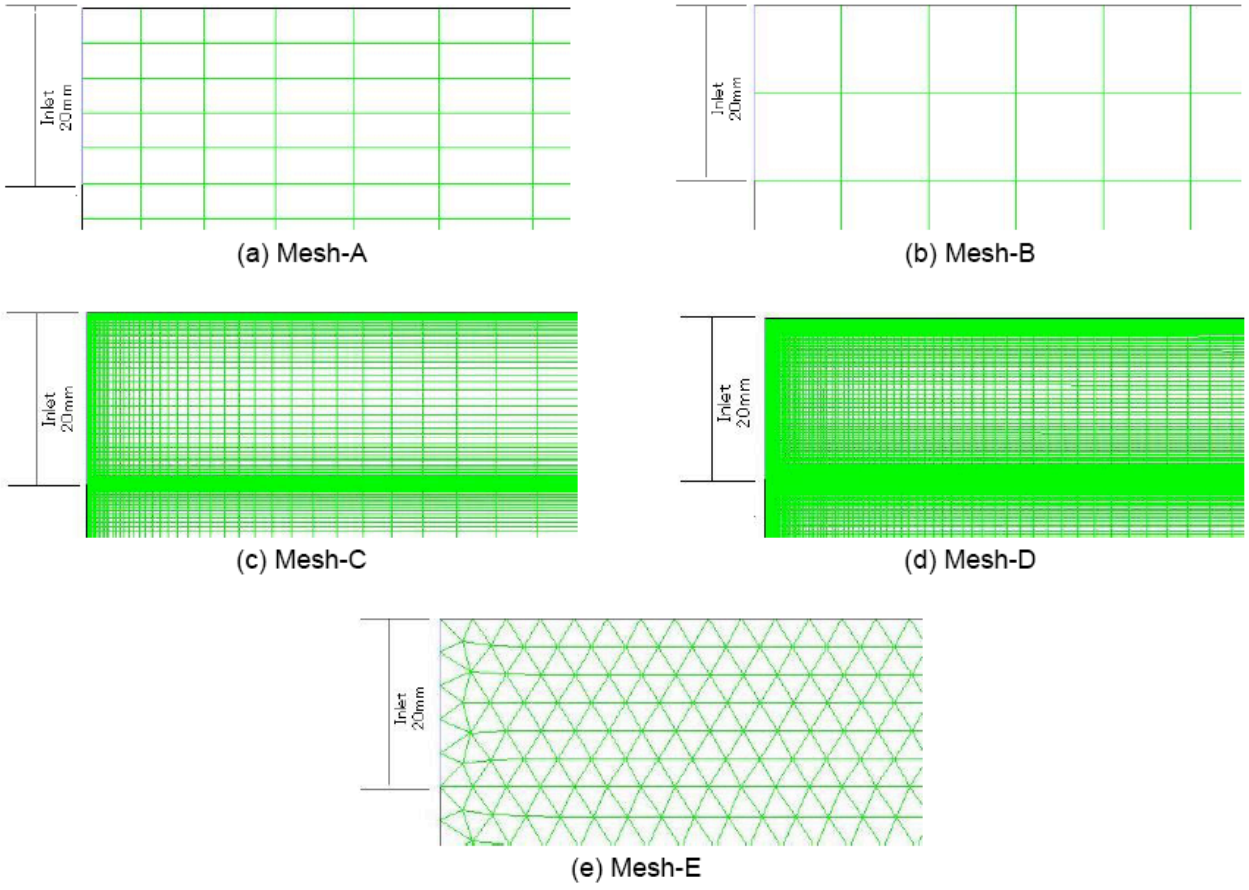

Figure 2: Mesh cell distribution around the inlet supply area for the different mesh designs Mesh-A through to Mesh-E.

errors, the high-order QUICK scheme was used for the advective term, and SIMPLE as the pressure-velocity coupling. For all other conditions, default values were used. In addition, to avoid solution errors resulting from incomplete convergence, a criterion on dimensionless residual errors was set to approximately $\leq 10^{-7}$.

3.2. Results for Mesh Dependence

The standard k-ε turbulence model was used in FLUENT to evaluate the different mesh configurations. Figure **3** shows the predicted results for the horizontal mean air velocity U, normal stress $\overline{u'^2}$, and Reynolds

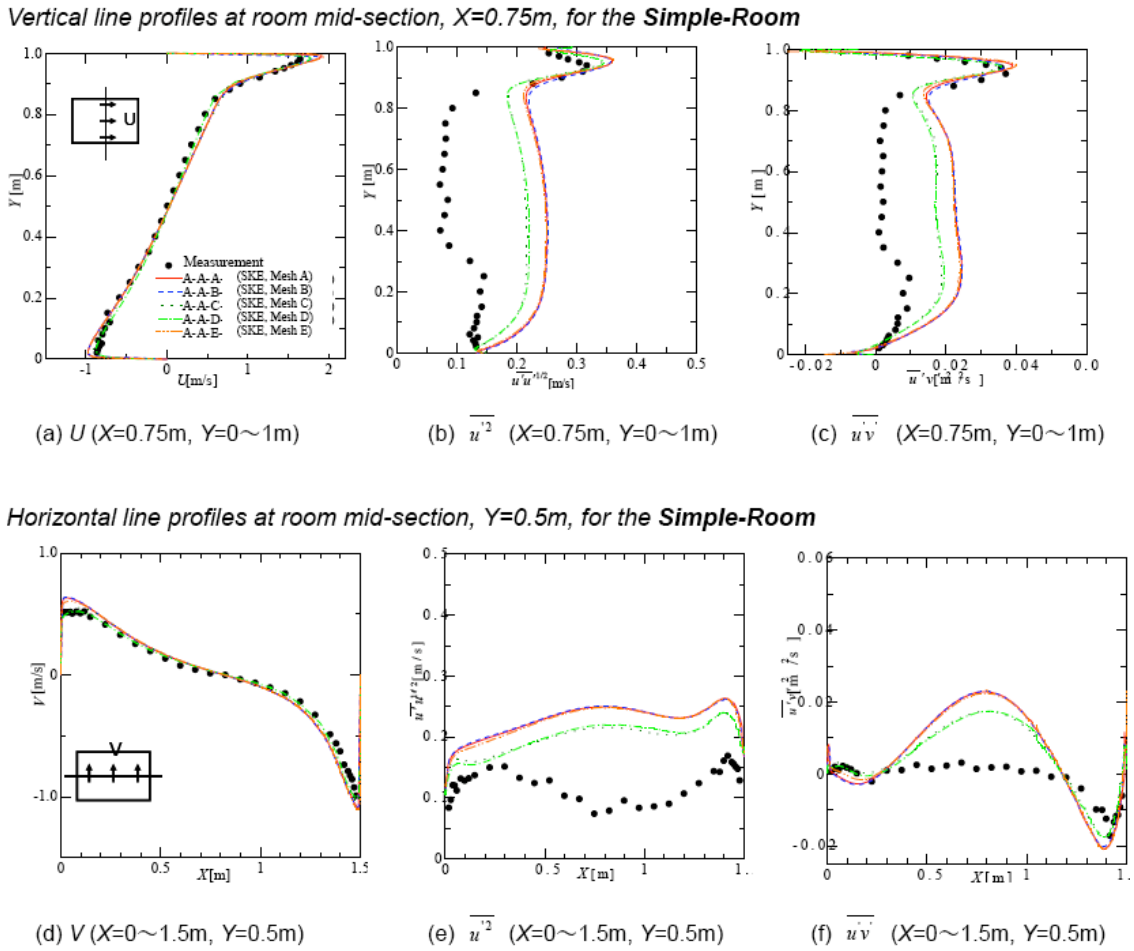

Figure 3: Influence of the mesh configuration evaluated using the standard-k- ε turbulence model in FLUENT (Code-A) on the Simple-Room scenario. Line profiles were taken at: the midsection of the room in the vertical axis, X=0.75m (a) U-velocity profile (b) normal stress and (c) Reynolds stress; and in the horizontal axis Y = 0.5m (d) V-velocity profile (e) normal stress, and (f) Reynolds stress.

stress $\overline{u'v'}$ on the mid-vertical line (X = 0.75 m, Y = 0-1.0 m) at the center position for the Simple-Room scenario. Similarly the profiles for the vertical mean wind speed and turbulent properties (V, $\overline{u'^2}$, $\overline{u'v'}$) were taken on the mid-horizontal line (X = 0-1.5 m, Y = 0.5 m). The values for $\overline{u'^2}$ and $\overline{u'v'}$ were calculated using the approximation formula of the eddy viscosity model.

There was no large variation due to mesh configuration for the Simple-Room scenario with the results capturing mean horizontal and vertical velocity components well (Figures 3a and 3d). At the supply inlet in Mesh B, we originally anticipated that the longitudinal coverage for the jet flow would be underestimated because only two cells were allocated vertically; however, no such result was observed. There is a possibility of mesh influence on overall flow field trends where strong circulation flows occur inside the room. With regard to $\overline{u'^2}$ and $\overline{u'v'}$, the increased number of cells for Mesh-E produced the same level of prediction accuracy as Mesh-A and Mesh-B (coarse mesh) in the low flow or stagnant region in the center of the room (Figures **3**(**b**), (**c**), (**e**), (**f**)).

The generalized logarithmic law or its corresponding wall function formula was adopted when the standard *k–ε* model was applied; however, no-slip (with linear law) wall boundary conditions were applied when we used Meshes C and D in accordance with the mesh size at the vicinity of wall surfaces, but the results showed that this was not a suitable grid design for turbulence models. Since the standard *k–ε* model contains no corrections for the decay in the eddy viscosity μ_t for the area around the wall surface, the predictions fail for the jet flow along the wall surface. However, the results showed that the mean flow velocities are captured.

3.3. Turbulence Model Performance

Figure **4** shows the results for the Simple-Room scenario where the predicted U and V velocities around

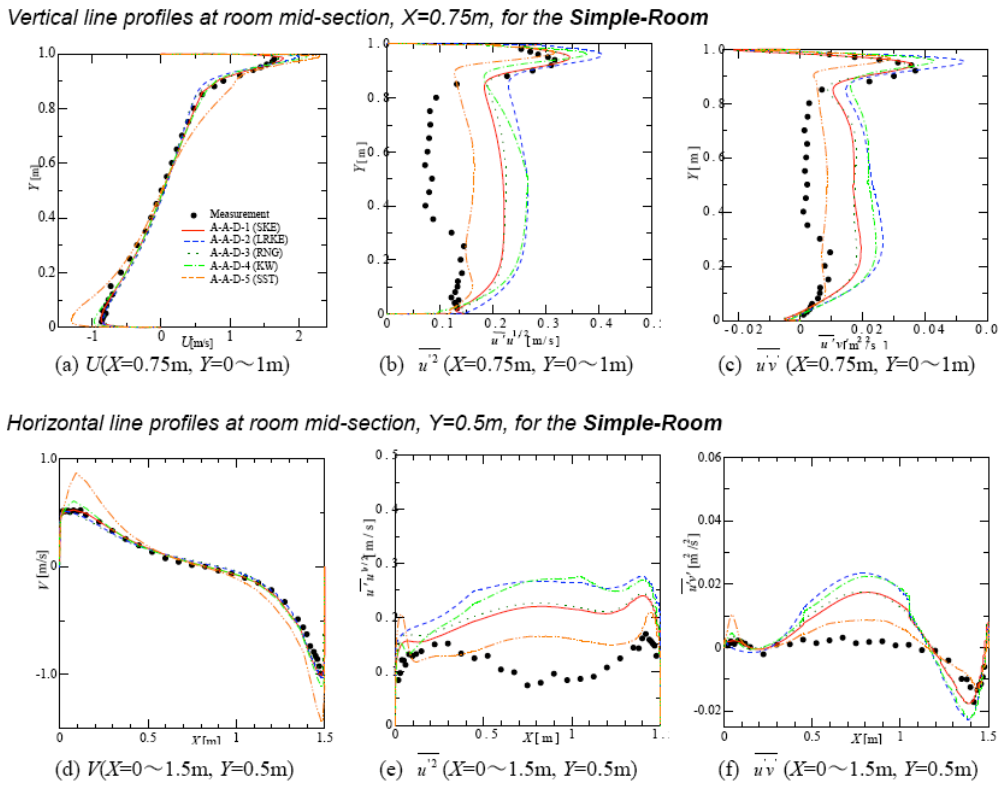

Figure 4: Influence of different turbulence models using FLUENT (Code-A) on the Simple-Room scenario with Mesh-D. Line profiles were taken at: the midsection of the room in the vertical axis, X=0.75m (**a**) U-velocity profile (**b**) normal stress and (**c**) Reynolds stress; and in the horizontal axis Y = 0.5m (**d**) V- velocity profile (**e**) normal stress, and (**f**) Reynolds stress.

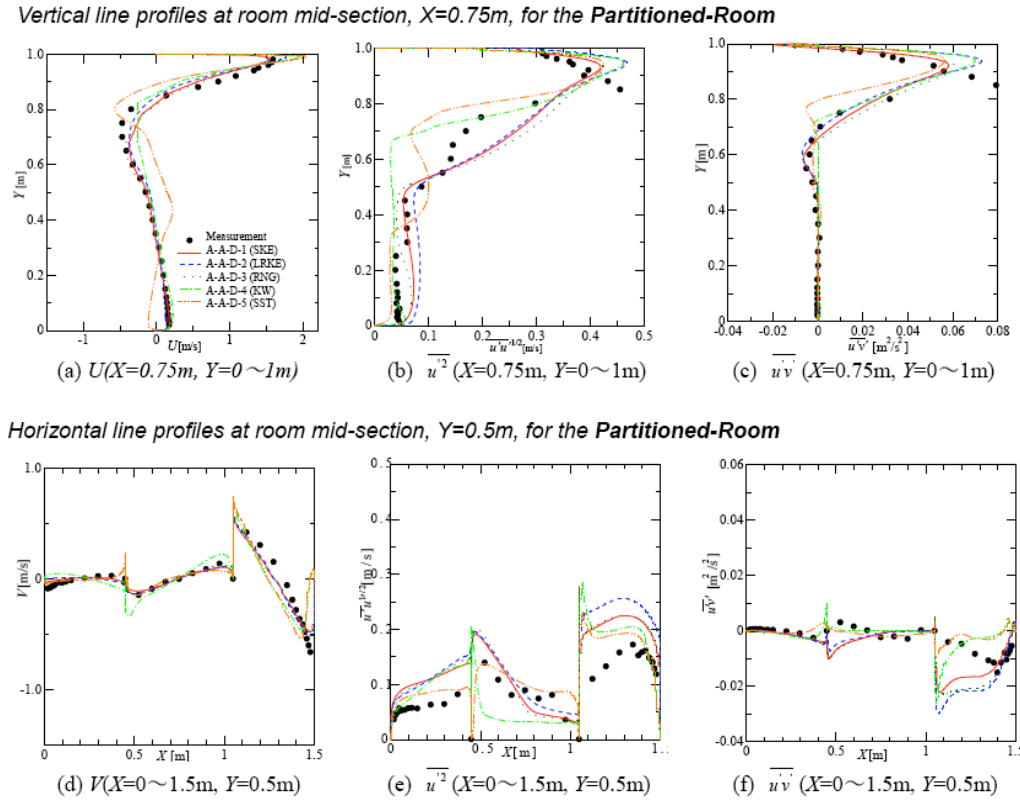

Figure 5: Influence of different turbulence models using FLUENT (Code-A) on the Partitioned-Room scenario with Mesh-D. Line profiles were taken at: the midsection of the room in the vertical axis, X=0.75m (**a**) U-velocity profile (**b**) normal stress and (**c**) Reynolds stress; and in the horizontal axis Y = 0.5m (**d**) V-velocity profile (**e**) normal stress, and (**f**) Reynolds stress.

the wall surface using the SST k–ω model are a little large compared with experimental values; the results for all other models are in good agreement with the experimental results (Figures **4**(**a**) and **4**(**d**)). The $\overline{u'^2}$ and $\overline{u'v'}$ results for each model conform to the experimental results at the area around the wall surface, but the models tended to overestimate compared with the experiment in the stagnant area in the center of the room (Figures **4**(**b**), (**c**), (**e**), (**f**)).

The same line profiles for the Simple-Room were applied to the Partitioned-Room scenario. Figure **5** shows the results for the Partitioned-Room. The predicted U profiles showed similar differences from the experimental results Figure **5**(**a**) as they did for the Simple-Room case. There were also problems in the reproducibility of the average wind speed for the area around the wall surface when using the SST k–ω model for both the Simple-Room and Partitioned-Room. We believe this was caused by the manner in which the blending function was handled when switching the k–ω model (inside the boundary layer) to the standard k–ε model (outside the boundary layer). The SST- k–ω produced the closest matching results to the experimental results in the detachment area at the top of the partition for $\overline{u'^2}$ and $\overline{u'v'}$ along the vertical line profile (Figure **5**(**e**), (**f**))

3.4. Comparisons Between Commercial CFD Codes

Figure **6** compares the results between four commercial CFD codes, FLUENT, CFX, STREAM, and Star-CD. The codes were used with the following turbulence models: the standard k–ε model, the low-Re

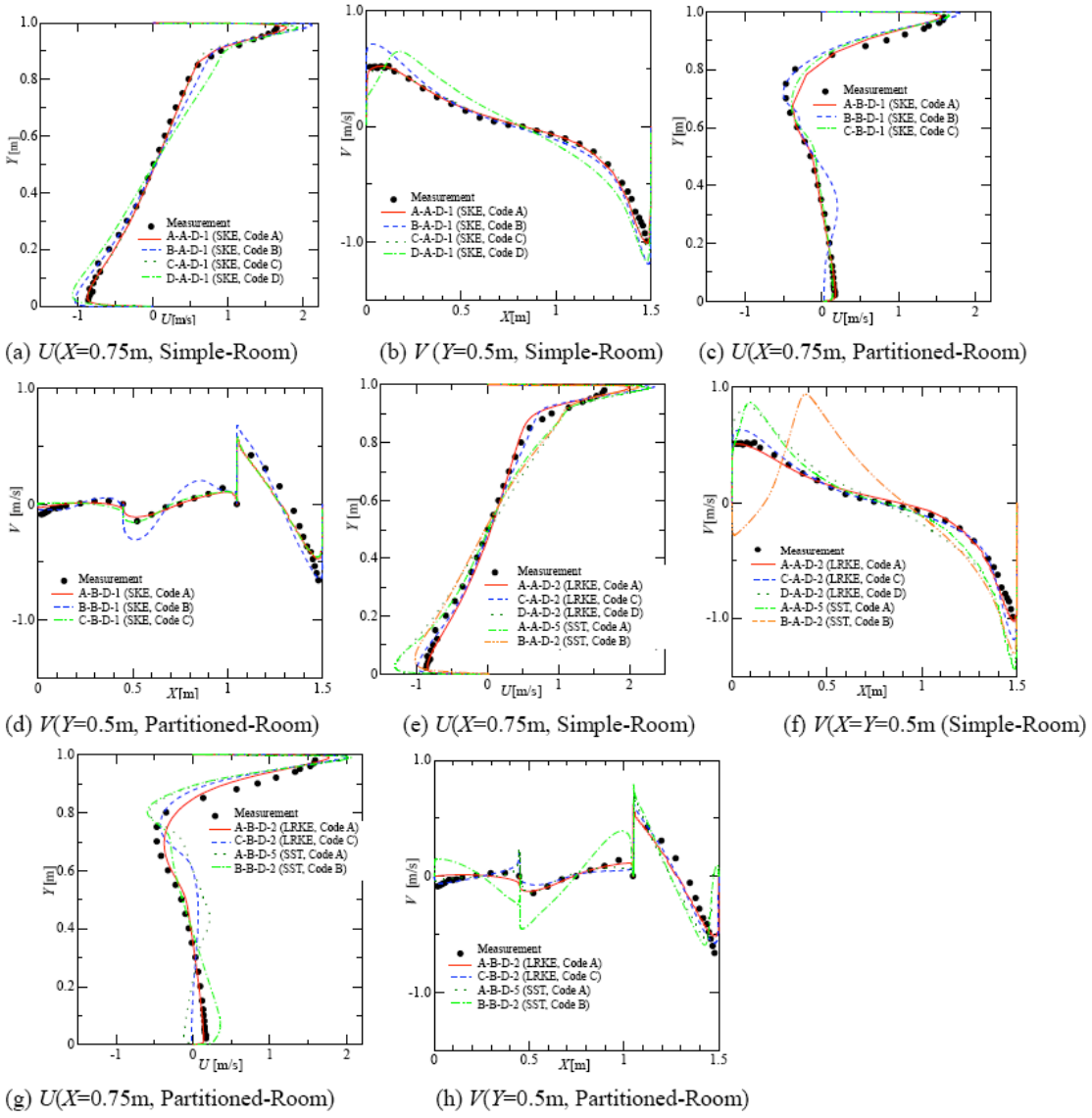

(a) U(X=0.75m, Simple-Room) (b) V (Y=0.5m, Simple-Room) (c) U(X=0.75m, Partitioned-Room)

(d) V(Y=0.5m, Partitioned-Room) (e) U(X=0.75m, Simple-Room) (f) V(X=Y=0.5m (Simple-Room)

(g) U(X=0.75m, Partitioned-Room) (h) V(Y=0.5m, Partitioned-Room)

Figure 6: Comparison between general-purpose CFD codes applied to Target A and Target B. The CFD codes are labelled as: Code A – FLUENT; Code B – CFX; Code C – STREAM; Code D – Star-CD.

k–ε model, and the SST k–ω model. In these tests, all other boundary conditions and numerical setup were set as similar as possible. For the Simple-Room (Figure **6**(**a**), (**b**), (**e**), (**f**)), the predictions of mean velocities varied greatly along the centerline (X=Y=0.5m), depending on the commercial CFD code being used. In particular, there were large fluctuations in reproducibility for flow fields around the wall surface. For the Partitioned-Room, slight differences between the CFD codes were observed (Figure **6**(**c**), (**d**), (**g**), (**h**)). In general the FLUENT, and CFX were able to capture the profiles the best. The greatest variation between the codes occurred mainly in the near wall regions.

3.5. Error Estimation and Convergence Tests

Errors that may occur in numerical analyses include solution errors (the difference between the true solution and the predicted numerical solution), truncation errors (errors due to discretization), dissipative, and dispersive errors. We focus on solution errors and show how the numerical settings affect the results. Figure **7** shows flow streamlines from FLUENT simulations using the standard k–ε model for the Simple-Room scenario. We started by setting all initial values for flow variables (U, V, W, k and ε) to zero and then performed steady-state analyses. Convergence test conditions varied slightly, depending on the CFD code that was used. For example, the convergence test conditions (residual error definition) for FLUENT were based on the preservation formula for the arbitrary variable numbers φ given in (1). Disequilibrium is defined in (2) as the total over all calculation cells P.

$$a_P\phi_P = \sum_{nb} a_{nb}\phi_{nb} + b \tag{1}$$

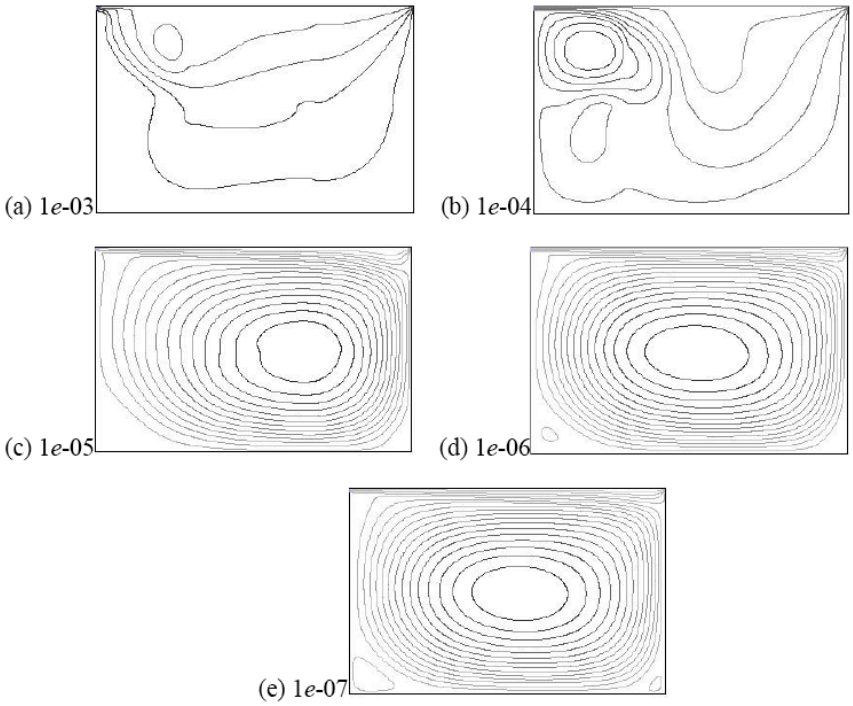

Figure 7: Streamline results for different residual convergence criteria using FLUENT.

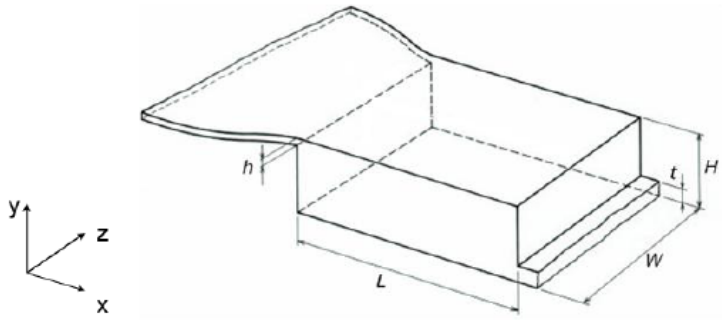

Figure 8: IEA Annex20 test case.

$$R^{\phi} = \sum_{cellsP} \left| \sum_{nb} a_{nb}\phi_{nb} + b - a_p\phi_p \right| \quad (2)$$

The residual defined in equation (2) was scaled as follows:

$$R^{\phi} = \frac{\sum_{cellsP} \left| \sum_{nb} a_{nb}\phi_{nb} + b - a_p\phi_p \right|}{\sum_{cellsP} \left| a_p\phi_p \right|} \quad (3)$$

Generally, default convergence conditions are set between about 10^{-3} and 10^{-4}; however, for this analysis, we set stricter conditions to 10^{-7}, which improved the predicted mean flow results to match closer with the experimental results. We found many cases in which the default values by the commercial CFD software were insufficient for convergence tests. This prompted stricter convergence conditions and the resulting flow field distribution from each case was compared to verify stability and accuracy.

4. RESULTS: IEA ANNEX-20 ROOM

4.1. Benchmark Test Against Isothermal IEA-Annex-20 Room Model

The IEA Annex20 room experimental data [31] was used to compare against the numerical results for isothermal airflow. Figure **8** shows a schematic where the room has a slot-type inlet and outlet. This test case is named IEA 2-D, although the geometry is 3D. The isothermal measured data were taken at the mid-plane cross-section (z = 1.5H) based on airflow velocities using laser Doppler Velocimetry (LDV). The dimensionless scales of the indoor space was h/H = 0.056, L/H = 3.0, t/H = 0.16. Additional details have been released online [31].

Since turbulence is inherently 3D in nature, the computational simulations were performed in both 2D and 3D and comparison with the experimental data were made on the mid-plane. Four turbulence models were evaluated using FLUENT – the standard k–ε model, low-Re k–ε model (Abe–Kondoh–Nagano model), standard k–ω model, and the SST k–ω model.

Two types of grid designs were used (Figure **9**). For the standard k–ε model a wall function was applied, while for the k–ω models, and low-Re k–ε model the near wall mesh fine enough to resolve the viscous sub-layer. These two grid design were both used in the SST k–ω model. The same grid designs for the x-y planes were applied to both the two- and three-dimensional analyses. Detailed Information for the numerical and boundary conditions are contained in Table **4**.

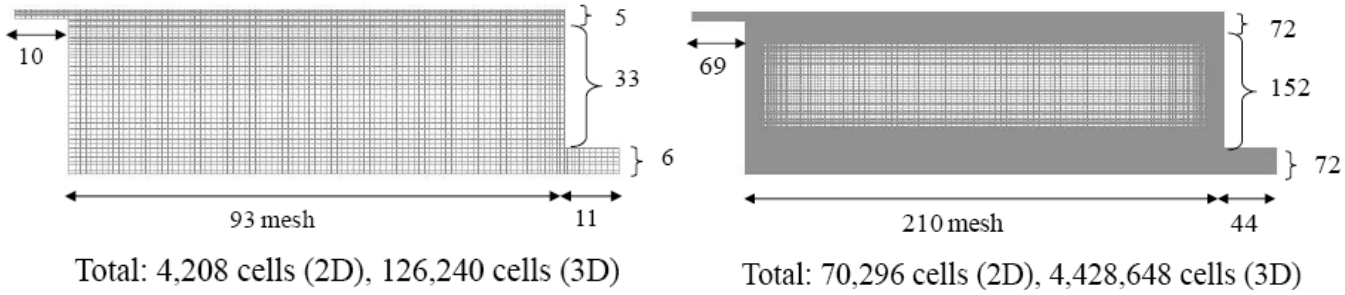

Figure 9: Computational mesh for the IEA Annex20 test case. (**a**) Mesh distribution/design used in the standard k–ε model. For the 3D model there were 30 cells in the z-direction. (**b**) Mesh distribution/design used in the low-Re k–ε model partition. For the 3D model there were 63 cells in the z-direction.

Table 4: Numerical and Boundary Condition Settings for the IEA-Annex 20 Room Model

Geometry	H=3.0 m, L=9.0 m, W=3.0 m, h=0.168 m, t=0.48 m
Inflow Condition of Experiment	U_{in} =0.455 m/s and TI= 4 %, (Corresponds to Re=$U_{in}h$/v=5000)
Mesh	Structured grid
Algorithm	SIMPLE
Scheme	QUICK for advection term
Inflow boundary	U_{in} =0.455 m/s, k_{in} =3/2× (U_{in}×0.1)^2, ε_{in} =$C_\mu^{3/4}$×$k_{in}^{3/2}$/l_{in}, C_μ=0.09, l_{in} =(1/10)h
Outflow boundary	U_{out} = free slip, k_{out}= free slip, ε_{out} = free slip
Wall treatment	Wall function (Generalized log law) for Standard k–ε fine near wall mesh for Low Re k–ε

4.2. Turbulence Model Comparisons

Figure **10** shows the results for velocity magnitude (scalar velocity) distributions for the turbulence models tested. A large circulating flow was produced from the supply inlet and exhaust outlet, and areas of stagnant flow formed in the center of the room. The size of the recirculation produced varied based on the turbulence model. This was especially true when the standard k–ω and the SST k–ω models were used. In these cases, circulation flows around the center of the floor surface separated from its surface which differed from what was found using the two k–ε models.

Velocity line profiles were taken along horizontal lines at a distance of $h/2$ from the ceiling, and floor, and vertical lines at a distance of $x = H$, and $x = 2H$ from the supply inlet. The results shown in Figure **11** are obtained from 2D computational models and compared with the 2D data measurements in the centre-plane of the IEA-Annex-20 room. Overall the velocity profiles from the standard k–ε and the low-Re k–ε models closely match the experimental results the best. Differences between the predicted velocities, particularly around the floor area, can be seen in the profiles for the line $x = H$, shown in Figure **11**(**a**). This is caused by the different predicted recirculation region that is formed inside the room from the different turbulence models. These differences correspond to the for velocity contour distribution shown in Figure **10**.

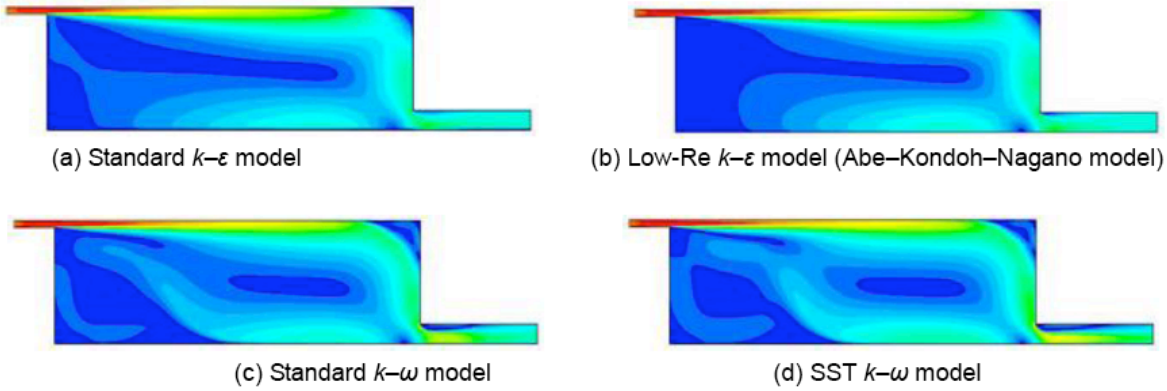

Figure 10: Scalar velocity distributions from each of four turbulence models.

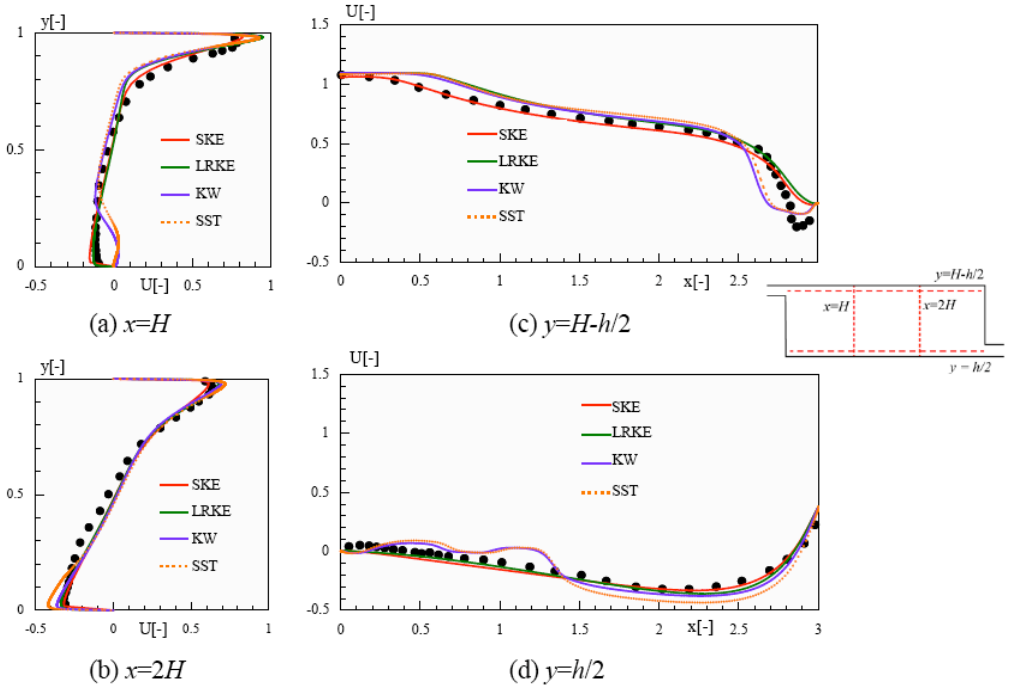

Figure 11: Velocity profiles taken along two horizontal (a,b) and two vertical (c,d) lines for different turbulence model simulations in 2D and compared with experimental data from the IEA-Annex-20 room.

Figure **12** shows the velocity profiles taken in the mid-plane for simulations run in a 3D room. Comparatively the standard k–ε and the low-Re k–ε models displayed similar results between a two- and three-dimensional case. However, the results from the SST k–ω model changed significantly, between the 2D and 3D models. Nevertheless, results from the three-dimensional analysis corresponded well with the experimental results.

5. RESULTS: NON-ISOTHERMAL ROOM AIRFLOW

5.1. Room Model of Murakami *et al*. [38]

In this section, we discuss CFD predictions of temperature and airflow distributions in rooms where horizontal non-isothermal air jets are supplied. Figure **13** shows a schematic of the room geometry. A horizontal inlet jet with a square supply inlet (dimensions of L_0 x L_0) in the center of the left wall supplies cold air into the room, instead of near the ceiling to avoid the Coanda effect. The opposing wall on the right is heated with four square outlets (dimensions of L_0 x L_0), each located in the corners of the wall. The remaining top, bottom, and side walls are all insulated (e.g. adiabatic conditions).

This room model is representative of fundamental analyses for air conditioning that involves a nozzle that supplies horizontal airflow into a space subjected to direct sunshine. Typically, a symmetrical boundary condition is used at the mid-plane to reduce the

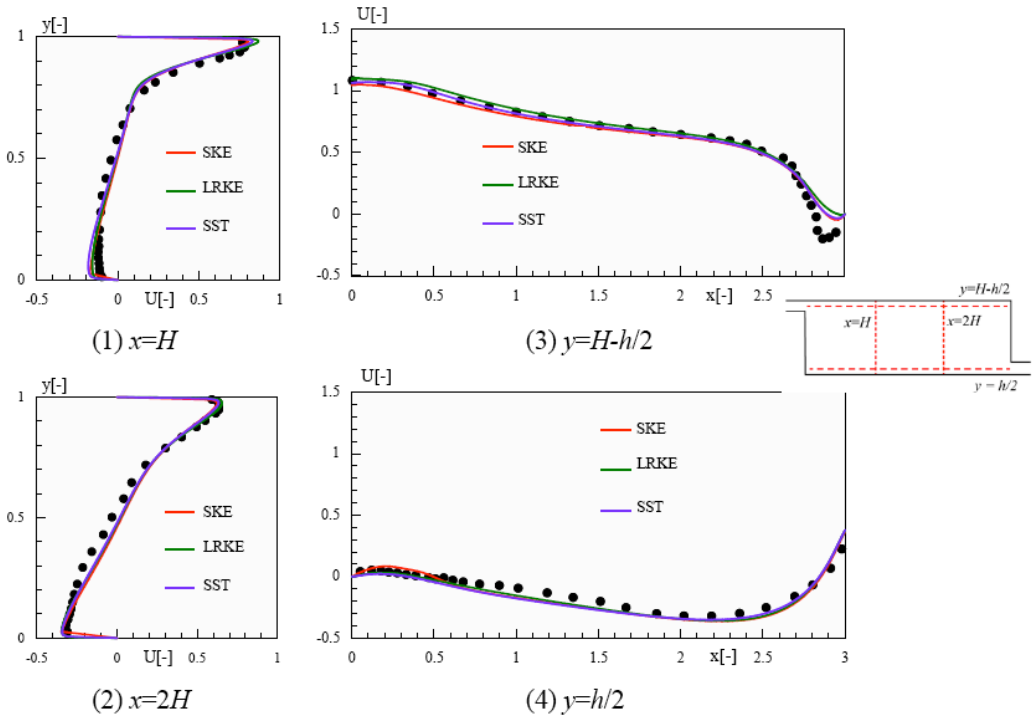

Figure 12: Velocity profiles taken along two horizontal (a,b) and two vertical (c,d) lines for different turbulence model simulations in 3D and compared with experimental data from the IEA-Annex-20 room.

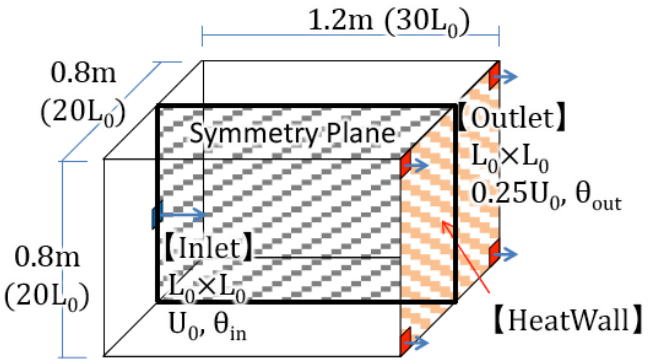

Figure 13: Schematic of room geometry that has cold inlet air entering from the left wall, and four outlets located in the corners of the opposing right wall.

computational analyses. In this study, the analyses of both half and the whole region was performed to determine the influence of the 3D turbulent flow structures with respect to the turbulence model used. Three commercially CFD software were used to determine their performance.

Murakami *et al*. [38] used this model in the late 1980s to perform a high-accuracy experiment, and in the 1990s, his research group were able to validate the accuracy of CFD results [38]. Turbulence model studies were performed based on this experiment which included Kato *et al*. [39] evaluating an algebraic stress model (ASM), Ooka *et al*. [40] evaluating a Differential Stress Model (DSM), and Mizutani, *et al*. [41] evaluating various LES models.

In this analysis, the room domain was non-dimensionalized by using representative velocity U_0 and length scale L_0. The air is assumed incompressible in the room, and dimensionless values based on Archimedes number, *Ar* are used. *Ar* is the ratio of gravitational forces to viscous forces and describes the relative strength of natural convection to forced convection. In previous experiments, measurements were performed using different values for *Ar* number as parameters, while in many simulation comparison studies *Ar* = 0.016 was used. The Archimedes number is defined by

$$Ar = \frac{g\beta\Delta T_0 L_0}{U_0^2} \quad (4)$$

However, since no dimensionless analysis can be performed using Star-CD and FlowDesigner, the non-dimensional values were restored to their corresponding dimensional values for analysis. Here, dimensionless Archimedes number *Ar* = 0.016 is used. Given T_0 = 12.2°C, L_0 = 0.04 m, and U_0 = 1.0 m/s, the following parameters are used: air jet velocity; *U* = 1.0 m/s, supply inlet size; 0.04 m × 0.04 m, inlet air temperature; 0°C, and exhaust outlet air temperature; 12.2°C. The amount of heat loss was computed on the basis of the airflow rate V_q [m^3/s], temperature difference ($\theta_o - \theta_i$) [K], and volumetric heat capacity for air $c_p\rho$ [J/m^3K]. The generated heat (calorific value) equivalent to the computed amount of heat loss was applied to the heating planes. Heat and fluid flow values are calculated shown in Table **5**. For Star-CD simulations, assuming that the heating plate was a heat-flow boundary, the condition, *q* = 37.19 W/m^2 was applied.

5.2. Influence of Mesh

Simulations to determine the influence of the mesh were performed using Star-CD. Three types of meshes were used (Figure **14**): coarse mesh (cell width = 1L_0), fine mesh (cell width = 0.5L_0), and very fine mesh (cell width = 0.25L_0), each of which had uniform cell width. A cell dimension of 0.5 was used for the outlet and inlet in the coarse mesh.

The standard *k*–ε model was used, SIMPLE for pressure-velocity coupling, and MARS (monotone

Table 5: Calculations for Heat Generation Rate

Flow rate	$V_q = 0.0016\,[m^3/s]$
Amt. of heat loss	$Q = V \times (\theta_0 - \theta_i) \times C_p\rho = 23.564[W]$
Heat generation	$q = 37.19\left[W/m^2\right]$

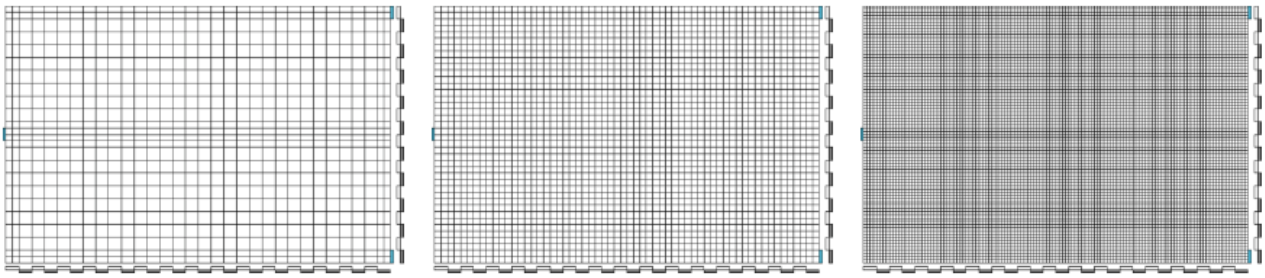

Figure 14: Three types of mesh design.

advection and reconstruction scheme) for the difference scheme. At the heating plate wall where E = 9.0, which is a model parameter of generalized log law is applied [33]. The physical fluid properties were set so that Re = 2,600 was achieved. A symmetrical boundary condition was applied in the mid-plane of the room so that only half the region was initially simulated. Afterwards, a full 3D model was simulated. The relaxation factors were lowered from its default values to ensure consistency in the solution between the analyses of the coarse and medium meshes – 0.3 for the advective term, 0.2 for the pressure term, and 0.5 for the temperature term. For the relaxation coefficients for the fine mesh, the default values for Star-CD were: 0.7 for the advective term, 0.5 for the pressure term 0.5, and 0.95 for the temperature term.

Figure **15** shows the computational time for each case with the result of the analysis on the whole region for comparison purposes. The computational time for the half region was slightly lesser than four minutes in the coarse mesh, whereas it took over two hours to

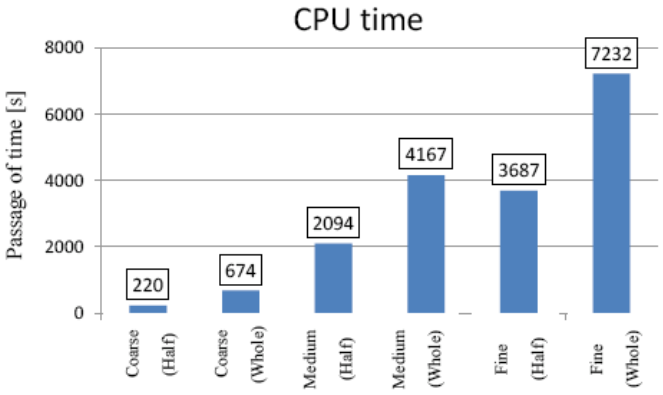

Table 5 No. of computations for each case

Case of Analysis	Iteration count
Coarse (half-region)	3,253
Coarse (whole-region)	5,000
Medium (half-region)	5,000
Medium (whole-region)	5,000
Fine half-region	1,000
Fine whole-region	1,000

* The analysis results for the whole region are shown for comparison purposes. The maximum iteration count was 5,000 for the coarse and fine meshes, and 1,000 for the very fine mesh. The convergence was set to 10^{-4} computation.

Figure 15: Computational time for each case (CPU time in second).

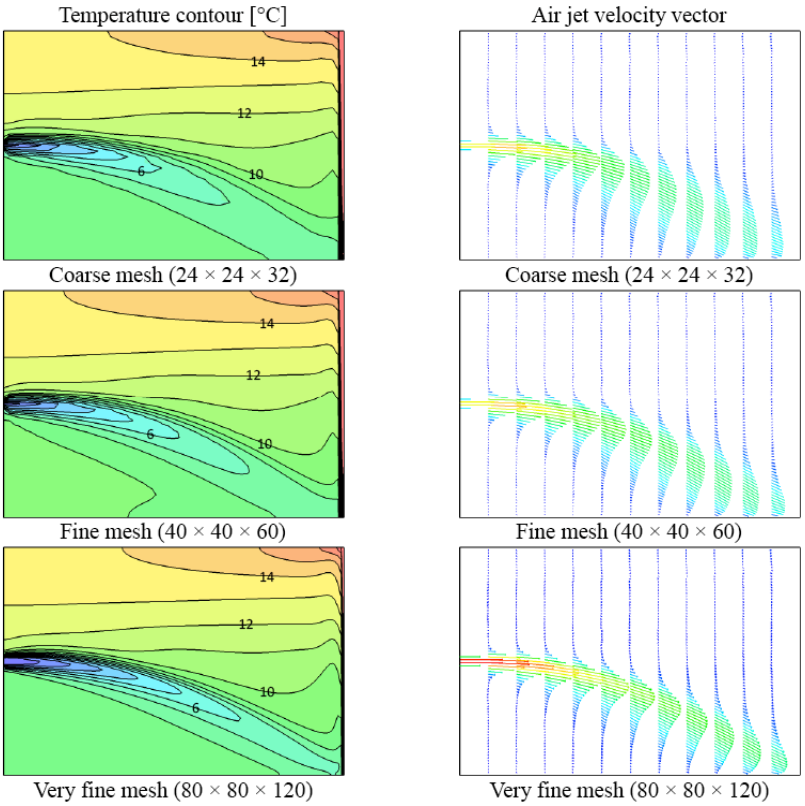

Figure 16: Results of analyses of each mesh type.

compute the whole region in the very fine mesh (Intel® Xeon, E2680× 2,+ Intel® Xeon, Phi 5110P, 256GB memory). For accuracy, the result of the very fine mesh best agreed with the experimental result. However, given that there were only minor differences in the computational results between meshes, resulting in relatively short time required to complete the analysis, the coarse mesh is most economical. In addition, only marginal difference was observed in the results between the whole and half regions when the solution satisfactorily converged in computation for them.

Figures **16-19** show the results for each mesh. Although the coarse mesh showed a high dispersion in temperature and air jet velocity, almost the same trends were observed in the results for all mesh sizes tested with the exception of a high dispersion in temperature and air jet velocity.

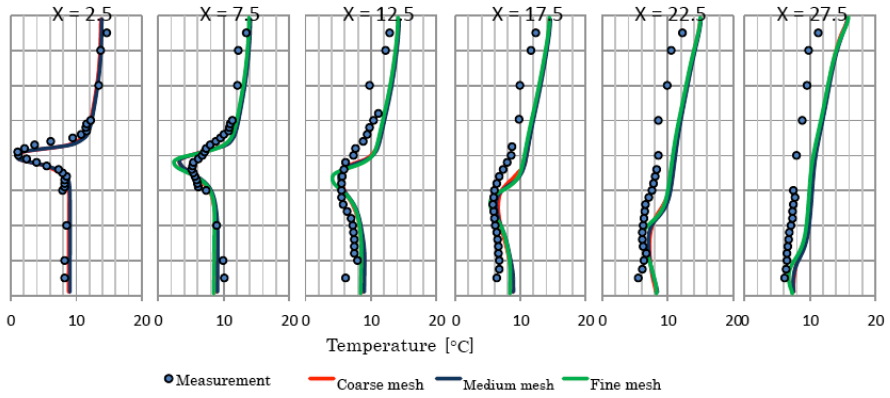

Figure 17: Temperature profiles.

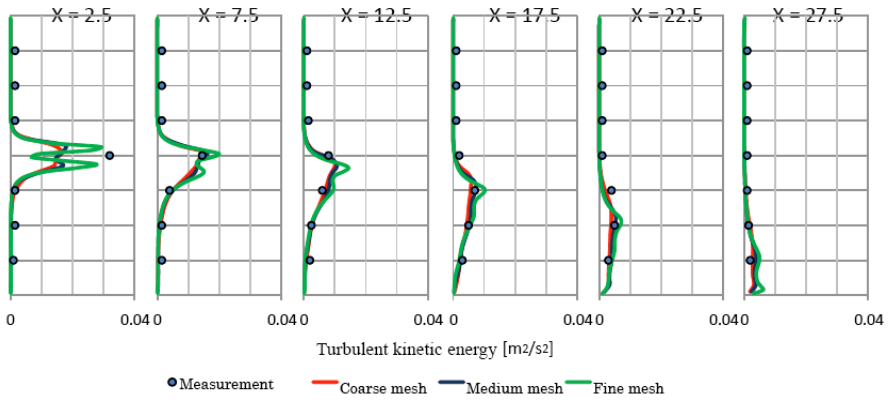

Figure 18: Turbulent kinetic energy profiles.

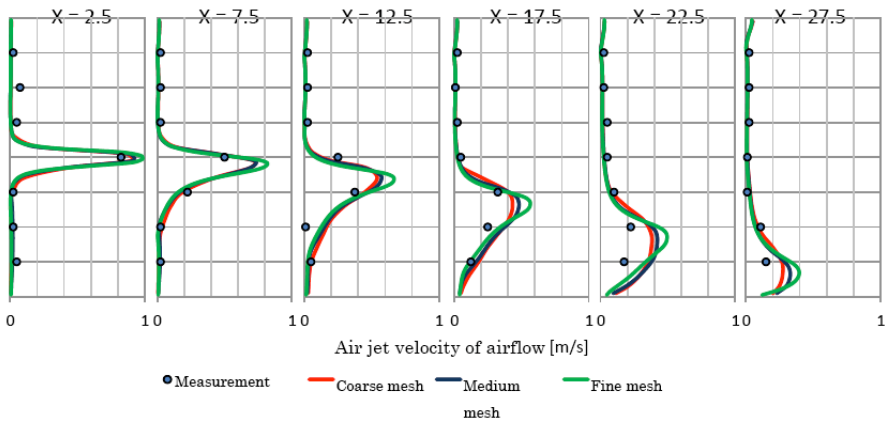

Figure 19: Scalar profiles of air jet velocity.

5.3. Turbulence Model Comparisons

Turbulence model performance for the standard k–ε and k–ω-SST, and Reynolds Stress Model (RSM), using Star-CD was validated. The validations used the medium mesh with the same settings used as in the previous section: SIMPLE for the algorithm and MARS for the advective term in the difference scheme. For all other terms, a central difference method was used. Assuming that the boundary condition for the wall plate was E = 9.0, a generalized log law was applied. With Re set to 2,600 and Ar to 0.016, the analysis was performed over the whole region.

The analysis results are shown in Figures **20-23** where the values are non-dimensionalized. The SKE and SST models produced approximately the same distributions. The RSM shows a greater decrease in air jet velocity than the other two models and overestimates the temperature in the area around the ceiling.

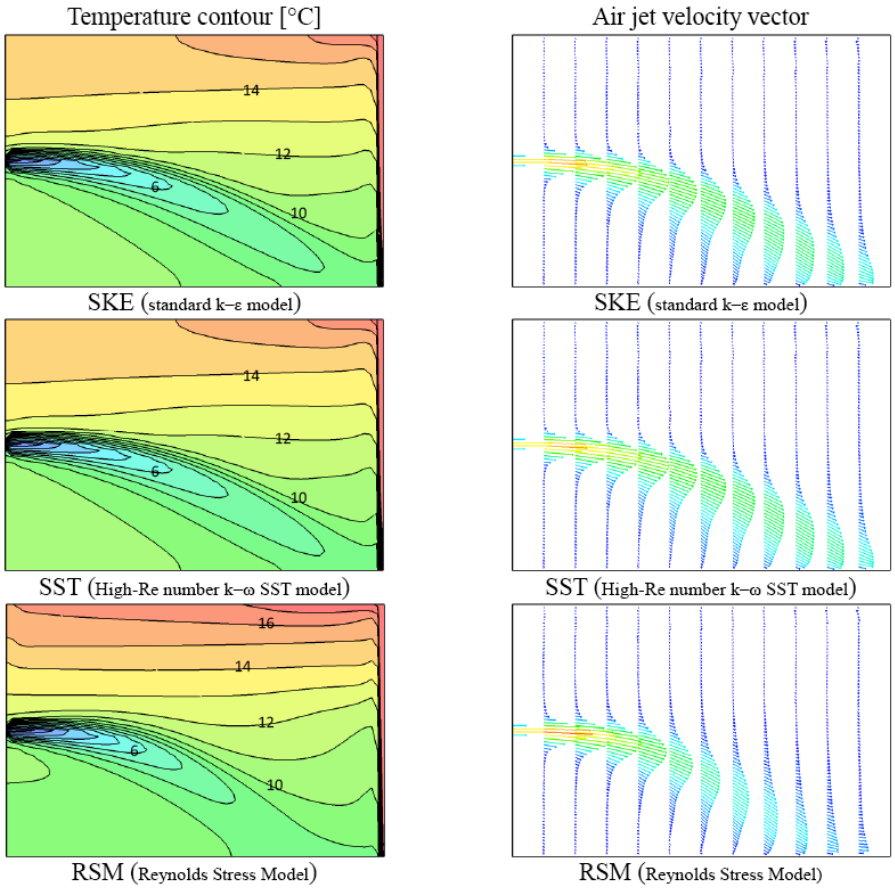

Figure 20: Analysis results (temperature distributions and air jet velocity vectors).

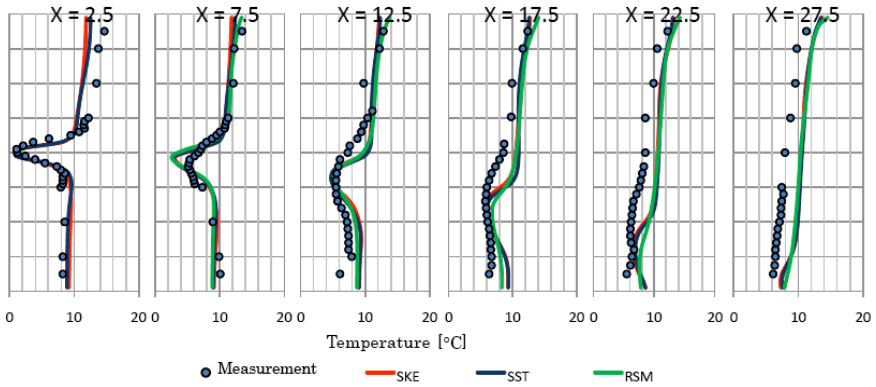

Figure 21: Temperature profiles.

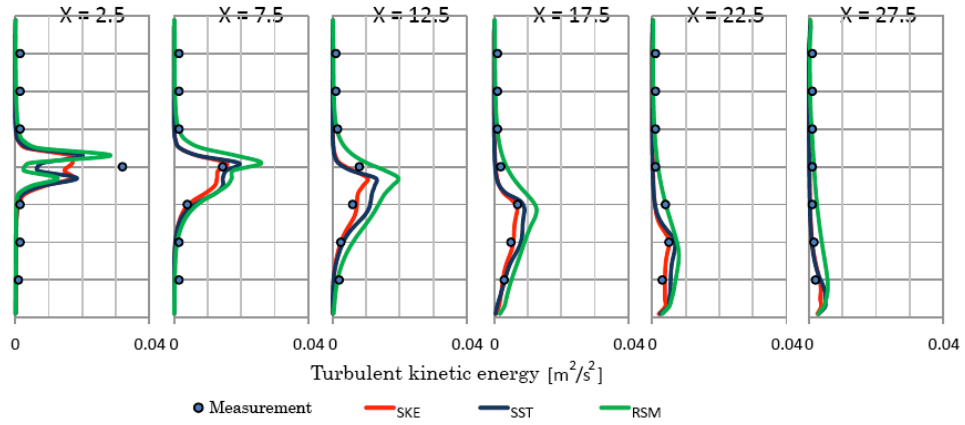

Figure 22: Turbulent kinetic energy profiles.

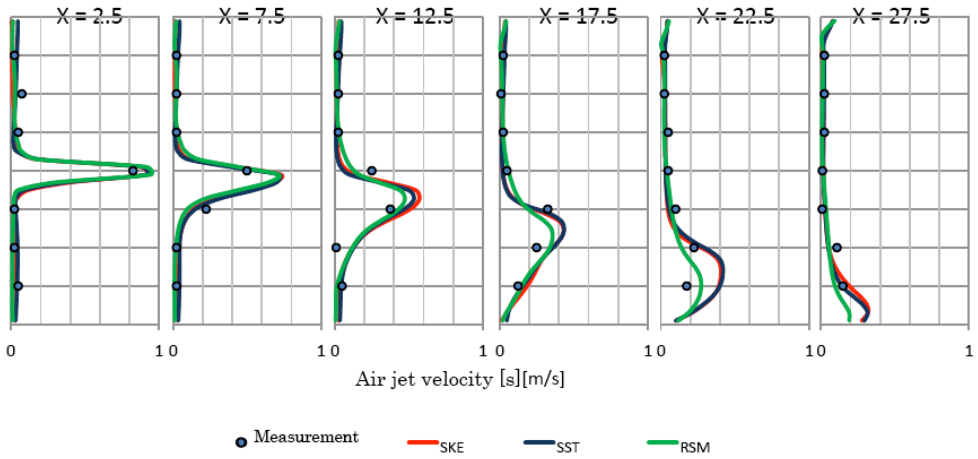

Figure 23: Scalar profiles of air jet velocity.

Table 6: Analysis Conditions used in each CFD Software Program

	STAR-CD (Code-D)	Open FOAM (Code-G)	Flow Designer (Code-H)
Turbulence Model	Standard k–ε model	Standard k–ε model	k–ε Model
Computational Algorithm	SIMPLE	SIMPLE	SIMPLE
Under relaxation (V, P, T)	V=0.7, P=0.3, T=0.95	V=0.4, P=0.4, T=0.4	V=1, P=0.8, T=1
Convergence Test	10^{-4}	10^{-5}	10^{-4}
Difference Scheme	UD	Upwind	1-Dimensional Upwind
Reynolds Number	2600	2670	2600
Mesh Partition	120×80×80	35×48×54	120×80×80

5.4. Comparisons Between CFD Software

Comparisons between three different CFD software were performed (STAR-CD (Code-D); Open FOAM (Code-G); and Flow Designer (Code-H)) with the conditions given in Table **6**. Default values in each software were used for the physical properties of air, so there were slight differences in Reynolds numbers. In the analysis using Code-G, the mesh was modified in the whole model compared to the half region model.

The results are shown in Figure **24** where Code-D show the lowest discrepancy in temperature and air jet velocity, the air jet reaching over a long distance in comparison with the other two CFD codes. Code-H shows a decrease in the momentum of the cold air. Comparing the results of these three software programs made it clear that slight differences in temperature contour were observed between them.

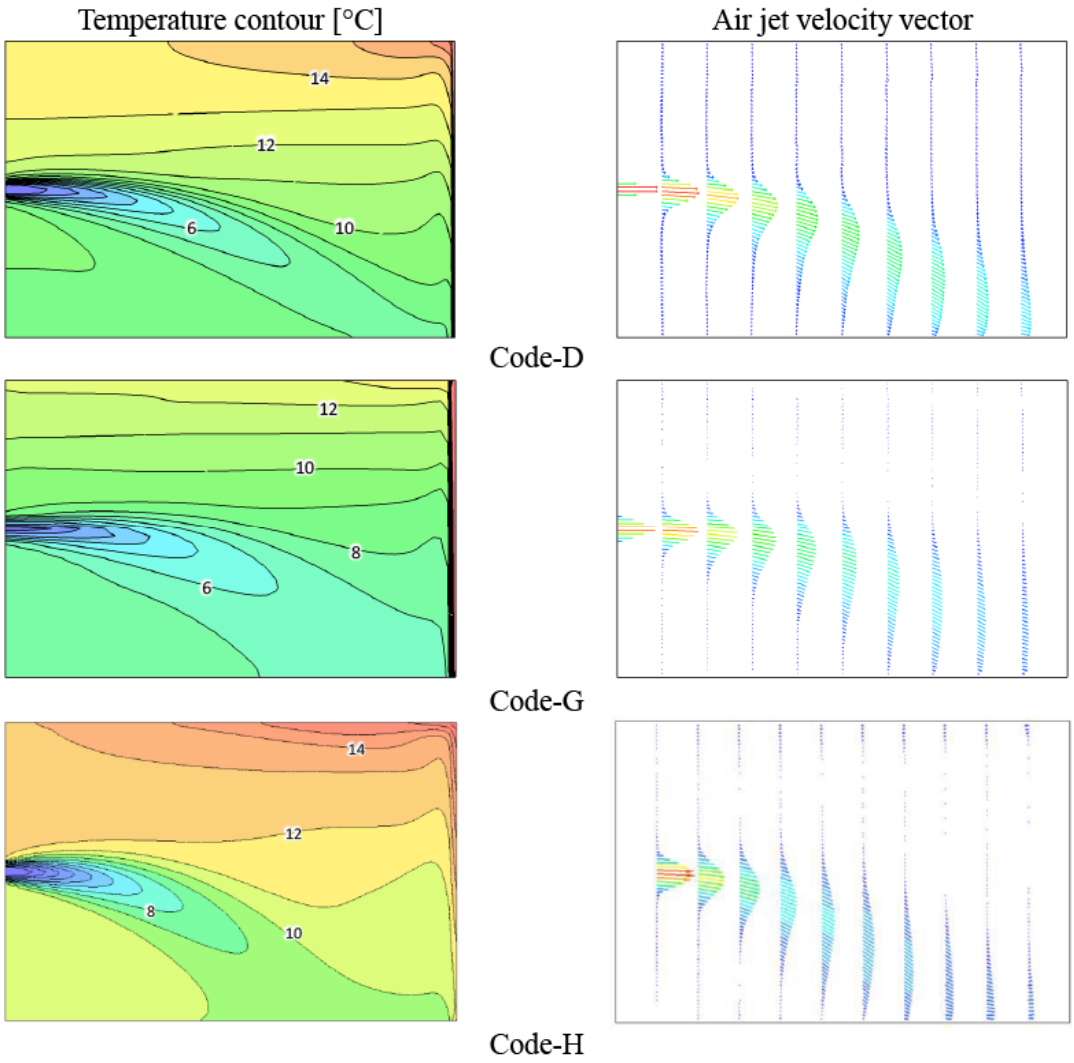

Figure 24: Analysis results (temperature contour and air jet velocity vector).

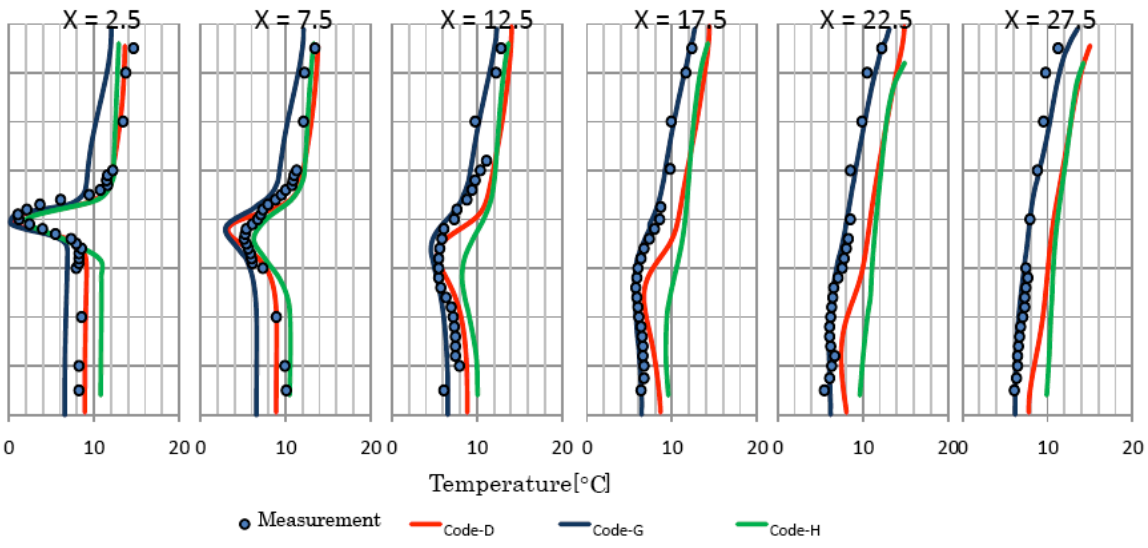

Figure 25: Temperature profiles.

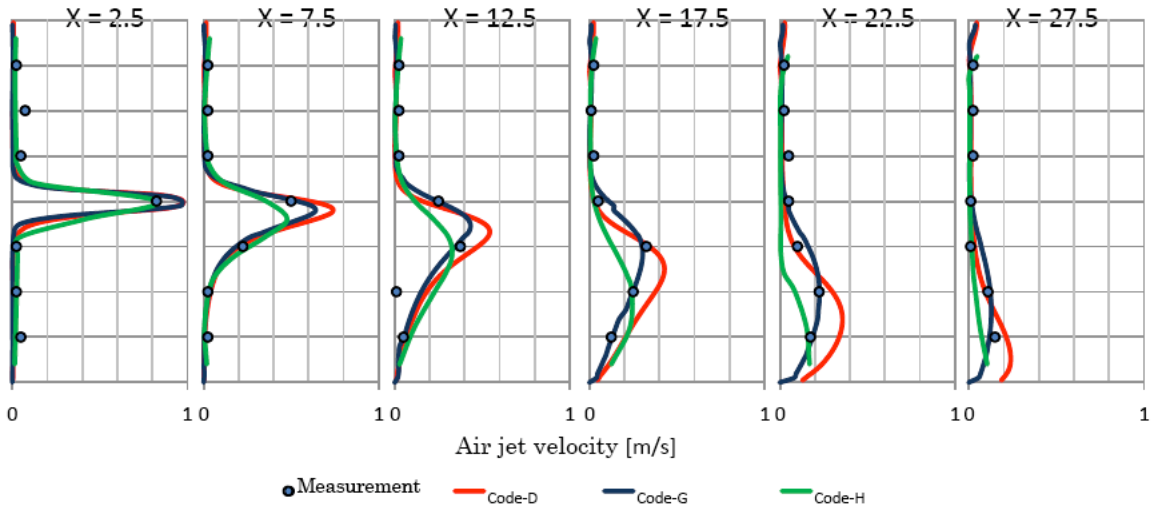

Figure 26: Scalar profiles of air jet velocity.

Figures **25** and **26** show the temperature and jet velocity profiles. Although the results for Code-G showed some discrepancy from the experimental near the inlet, the overall distribution agreed very well. Code-D and Code-H achieved similar profiles in the vicinity of the outlet, and the results were progressively worse further away from the inlet (e.g. approaching the heated plate side).

6. DISCUSSIONS

The commercial CFD code comes equipped with a user-friendly GUI and pre / post processing functions that can guide the user to consistent results even if the user is not familiar with settings for boundary conditions or differences in numerical algorithms. However, there are considerable possibilities in the selection of turbulence models and convergence criterions, even for flow field analyses of the relatively simple 2D room model. Consequently, care and attention is needed to perform an analysis that provides sufficient reproducibility. Obtaining accurate spatial distributions of mean flows is important for indoor analyses used on a practical level. Moreover, to estimate critical turbulence phenomena, it is also important to achieve very high accuracy in computing 2D normal and Reynolds stresses. In the evaluations presented here, sufficient accuracy was attained for mean flow patterns with all turbulence models used. However, the calculated normal and Reynolds stresses showed some differences compared with experimental results.

The purpose of applying CFD is to obtain a high level of validation. Therefore, to perform numerical analyses with high reliability, it is important to place quantitative restrictions on the margin of error attributed to numerical analysis. Consequently, we recommend a basic approach in which (a) an exploratory analysis is first performed using a coarse mesh design, then (b) a fine mesh is generated in a two-stage analysis to perform a full-scale analysis. We believe that changes in numerical solutions due to mesh types are reflected by changes in solution error associated with the changes in analysis mesh intervals. Furthermore, it should be possible to quantify the extent (degree) of those errors. In addition, we expect improvements in the level of convergence using results from exploratory analyses as restart files (initial value file) in mesh analyses.

To carry out CFD analyses with high reproducibility, evaluation and consideration are both needed, at the very least, for (1) exploring input conditions (including an appropriate selection for the turbulence model), (2) confirming the degree (level) of grid dependence, and (3) selecting appropriate convergence criteria. In complex situations that involve such complications as temperature fields and contaminant diffusion fields, a comprehensive description of the indoor environment requires not only a numerical algorithm for solving the Navier–Stokes equation, but also technology that pertains to each kind of scalar transport equation, possibly including considerations for radiation.

7. CONCLUSIONS

In this study, the dependences of mesh size, turbulence model, and commercial CFD software were verified. The high Re k-ε model achieved a reasonable degree of results even for the coarse mesh by reducing the relaxation coefficient. The total number of mesh largely affects computational time. For this reason, it

may be practically preferable that the number of mesh is set to the lowest possible value without impairing the accuracy of the analysis. Evaluation using different CFD software programs on a non-isothermal room airflow showed differences in temperature distributions between Code-D and Code-H and the experimental results increased at the measuring point closer to the heating plate. Thus, further study is needed for improving the boundary conditions of the heating plate. The results obtained from Code-G were closest to those of experiments. However, since some factors were ignored, such as the buoyancy production term, further discussions of the analysis method will be necessary.

NOMENCLATURE

U : average velocity in *X* direction [m/s]

V : average velocity in *Y* direction [m/s]

W : average velocity in *Z* direction [m/s]

u' : fluctuating velocity in *X* direction [m/s]

v' : fluctuating velocity in *Y* direction [m/s]

w' : fluctuating velocity in *Z* direction [m/s]

$\overline{u'^2}$: normal stress [m^2/s^2]

$\overline{u'v'}$: Reynolds stress [m^2/s^2]

g : acceleration of gravity [m/s^2]

k : turbulent kinetic energy [m^2/s^2]

T_0 : representative temperature [K]

L_0 : representative length scale [m]

U_0 : representative velocity [m/s]

V_p : air flow rate [m^3/s]

Re : Reynold number [-]

Ar : Archimedes number [-]

X : coordinate and distance

Y : coordinate and distance

y+ : dimensionless distance to wall (wall unit) [-]

TI : turbulence intensity [-]

E : coefficient in generalized log law (E=9.0)

β : volume expansion coefficient [1/K]

v : kinematic viscosity [m^2/s]

v_t : turbulent kinematic viscosity [m^2/s]

ρ : air density [kg/m^3]

ε : dissipation rate of turbulent kinetic energy [m^2/s^3]

ω : dissipation rate [s^{-1}]

APPENDIX – GOVERNING EQUATIONS FOR EACH TURBULENCE MODEL AND MODEL PARAMETERS

Turbulenc model	Governing equations and model functions
Std. *k-ε*	$\frac{\partial \rho k}{\partial t}+\overline{U_i}\frac{\partial \rho k}{\partial x_i}=\mu_t\left(\frac{\partial \overline{U_i}}{\partial x_j}+\frac{\partial \overline{U_j}}{\partial x_i}\right)\frac{\partial \overline{U_i}}{\partial x_j}+\frac{\partial}{\partial x_j}\left\{\left(\mu+\frac{\mu_t}{\sigma_\varepsilon}\right)\frac{\partial k}{\partial x_j}\right\}-\rho\varepsilon,$ $\frac{\partial \rho \varepsilon}{\partial t}+\overline{U_i}\frac{\partial \rho \varepsilon}{\partial x_i}=C_{\varepsilon 1}\frac{\varepsilon}{k}\mu_t\left(\frac{\partial \overline{U_i}}{\partial x_j}+\frac{\partial \overline{U_j}}{\partial x_i}\right)\frac{\partial \overline{U_i}}{\partial x_j}+\frac{\partial}{\partial x_j}\left\{\left(\mu+\frac{\mu_t}{\sigma_\varepsilon}\right)\frac{\partial \varepsilon}{\partial x_j}\right\}-\rho C_{\varepsilon 2}\frac{\varepsilon^2}{k}$
	$\mu_t=\rho C_\mu\frac{k^2}{\varepsilon}, C_\mu, C_{\varepsilon 1}, C_{\varepsilon 2}, \sigma_k, \sigma_\varepsilon$ (Model parameters)	
Low Re *k-ε*	$\frac{\partial \rho k}{\partial t}+\overline{U_i}\frac{\partial k}{\partial x_i}=\mu_t\left(\frac{\partial \overline{U_i}}{\partial x_j}+\frac{\partial \overline{U_j}}{\partial x_i}\right)\frac{\partial \overline{U_i}}{\partial x_j}+\frac{\partial}{\partial x_j}\left\{\left(\mu+\frac{\mu_t}{\sigma_\varepsilon}\right)\frac{\partial k}{\partial x_j}\right\}-\rho\varepsilon,$ $\frac{\partial \rho \varepsilon}{\partial t}+\overline{U_i}\frac{\partial \rho \varepsilon}{\partial x_i}=C_{\varepsilon 1}\frac{\varepsilon}{k}\mu_t\left(\frac{\partial \overline{U_i}}{\partial x_j}+\frac{\partial \overline{U_j}}{\partial x_i}\right)\frac{\partial \overline{U_i}}{\partial x_j}+\frac{\partial}{\partial x_j}\left\{\left(\mu+\frac{\mu_t}{\sigma_\varepsilon}\right)\frac{\partial \varepsilon}{\partial x_j}\right\}-\rho C_{\varepsilon 2}f_\varepsilon\frac{\varepsilon^2}{k}$ 8
	$\mu_t=\rho C_\mu f_\mu\frac{k^2}{\varepsilon}, f_\varepsilon=\left\{1-\exp\left(-\frac{y^*}{3.1}\right)\right\}^2\left[1-0.3\exp\left\{-\left(\frac{R_t}{6.5}\right)^2\right\}\right], f_\mu=\left\{1-\exp\left(-\frac{y^*}{14}\right)\right\}^2\left[1+\left(\frac{5}{R_t^{3/4}}\right)\exp\left\{-\left(\frac{R_t}{200}\right)^2\right\}\right], y^*=\frac{u_\varepsilon y}{\nu}, R_t=\frac{k^2}{\nu\varepsilon}, u_\varepsilon=(\nu\varepsilon)^{1/4}$	
	$C_\mu, C_{\varepsilon 1}, C_{\varepsilon 2}, \sigma_k, \sigma_\varepsilon$ (Model parameters)	

$$\frac{\partial \rho k}{\partial t}+\overline{U}_i\frac{\partial \rho k}{\partial x_i}=\mu_t\left(\frac{\partial \overline{U}_i}{\partial x_j}+\frac{\partial \overline{U}_j}{\partial x_i}\right)\frac{\partial \overline{U}_i}{\partial x_j}+\frac{\partial}{\partial x_j}\alpha_k(\mu+\mu_t)\frac{\partial k}{\partial x_j}-\rho\varepsilon,\qquad \frac{\partial \rho \varepsilon}{\partial t}+\overline{U}_i\frac{\partial \rho \varepsilon}{\partial x_i}=C_{\varepsilon 1}\frac{\varepsilon}{k}\mu_t\left(\frac{\partial \overline{U}_i}{\partial x_j}+\frac{\partial \overline{U}_j}{\partial x_i}\right)\frac{\partial \overline{U}_i}{\partial x_j}+\frac{\partial}{\partial x_j}\alpha_\varepsilon(\mu+\mu_t)\frac{\partial \varepsilon}{\partial x_j}-\rho C^*_{\varepsilon 2}\frac{\varepsilon^2}{k}$$

RNG k-ε $$\mu_t=\rho C_\mu\frac{k^2}{\varepsilon},C^*_{\varepsilon 2}=C_{\varepsilon 2}+\frac{C_\mu\eta^3(1-\eta/\eta_0)}{1+\beta\eta^3},\eta\equiv\frac{Sk}{\varepsilon},S\equiv\sqrt{2S_{ij}S_{ij}},S_{ij}=\frac{1}{2}\left(\frac{\partial \overline{U}_i}{\partial x_j}+\frac{\partial \overline{U}_j}{\partial x_i}\right),\left|\frac{\alpha-1.3929}{\alpha_0-1.3929}\right|^{0.3679}\left|\frac{\alpha+2.3929}{\alpha_0+2.3929}\right|^{0.3679}=\frac{\mu+\mu_t}{\mu}$$

$$C_\mu,C_{\varepsilon 1},C_{\varepsilon 2},\eta_0,\beta \qquad \text{(Model parameters)}$$

$$\frac{\partial \rho k}{\partial t}+\overline{U}_i\frac{\partial \rho k}{\partial x_i}=\mu_t\left(\frac{\partial \overline{U}_i}{\partial x_j}+\frac{\partial \overline{U}_j}{\partial x_i}\right)\frac{\partial \overline{U}_i}{\partial x_j}+\frac{\partial}{\partial x_j}\left\{\left(\mu+\frac{\mu_t}{\sigma_k}\right)\frac{\partial k}{\partial x_j}\right\}-\rho\beta^* f_{\beta^*}k\omega,\frac{\partial \rho \omega}{\partial t}+\overline{U}_i\frac{\partial \rho \omega}{\partial x_i}=\alpha\frac{\omega}{k}\mu_t\left(\frac{\partial \overline{U}_i}{\partial x_j}+\frac{\partial \overline{U}_j}{\partial x_i}\right)\frac{\partial \overline{U}_i}{\partial x_j}+\frac{\partial}{\partial x_j}\left\{\left(\mu+\frac{\mu_t}{\sigma_\varepsilon}\right)\frac{\partial \omega}{\partial x_j}\right\}-\rho\beta f_\beta\omega^2$$

$$\mu_t=\rho\alpha^*\frac{k}{\omega},\alpha^*=\alpha_\infty{}^*\left(\frac{\alpha_0{}^*+\mathrm{Re}_t/R_k}{1+\mathrm{Re}_t/R_k}\right),\alpha=\frac{\alpha_\infty}{\alpha^*}\left(\frac{\alpha_0+\mathrm{Re}_t/R_\omega}{1+\mathrm{Re}_t/R_\omega}\right),\alpha_0{}^*=\frac{\beta_i}{3},\mathrm{Re}_t=\frac{\rho k}{\mu\omega},f_{\beta^*}=1(\chi_k\le 0),f_{\beta^*}=\frac{1+680\chi_k{}^2}{1+400\chi_k{}^2}(\chi_k>0),\chi_k=\frac{1}{\omega^3}\frac{\delta k}{\delta x_j}\frac{\delta \omega}{\delta x_j}$$

Std. k-ω

$$\beta^*=\beta_i^*\left[1+\zeta^*F(M_t)\right],\beta_i^*=\beta_\infty{}^*\left[\frac{4/15+(\mathrm{Re}_t/R_\beta)^4}{1+(\mathrm{Re}_t/R_\beta)^4}\right],f_\beta=\frac{1+70\chi_\omega}{1+80\chi_\omega},\chi_\omega=\left|\frac{\Omega_{ij}\Omega_{jk}S_{ki}}{(\beta_\infty{}^*\omega)^3}\right|,\beta=\beta_i\left[1-\frac{\beta_i^*}{\beta_i}\varsigma^*F(M_t)\right],F(M_t)=0(M_t\le M_{t0})$$

$$F(M_t)=M_t{}^2-M_{t0}{}^2(M_t>M_{t0}),M_t^2\equiv\frac{2k}{a^2},R_k,\beta_i^*,R_\omega,\zeta^*,R_\beta,\beta_\infty{}^*,\alpha_\infty{}^*,\alpha_\infty,\alpha_0,M_{t0},\sigma_k,\sigma_\varepsilon \qquad \text{(Model parameters)}$$

$$\frac{\partial \rho k}{\partial t}+\overline{U}_i\frac{\partial \rho k}{\partial x_i}=\min\left(\mu_t\left(\frac{\partial \overline{U}_i}{\partial x_j}+\frac{\partial \overline{U}_j}{\partial x_i}\right)\frac{\partial \overline{U}_i}{\partial x_j},10\rho\beta^*k\omega\right)+\frac{\partial}{\partial x_j}\left\{\left(\mu+\frac{\mu_t}{\sigma_k}\right)\frac{\partial k}{\partial x_j}\right\}-\rho\beta^*k\omega$$

$$\frac{\partial \rho \omega}{\partial t}+\overline{U}_i\frac{\partial \rho \omega}{\partial x_i}=\rho\alpha\left(\frac{\partial \overline{U}_i}{\partial x_j}+\frac{\partial \overline{U}_j}{\partial x_i}\right)\frac{\partial \overline{U}_i}{\partial x_j}+\frac{\partial}{\partial x_j}\left\{\left(\mu+\frac{\mu_t}{\sigma_\varepsilon}\right)\frac{\partial \omega}{\partial x_j}\right\}-\rho\beta\omega^2+2\left(1-F_1\right)\sigma_{\omega,2}\frac{1}{\omega}\frac{\partial k}{\partial x_j}\frac{\partial \omega}{\partial x_j},$$

SST k-ω $$\mu_t=\frac{\rho k}{\omega}\frac{1}{\max\left[\frac{1}{\alpha^*},\frac{\Omega F_2}{a_1\omega}\right]},\sigma_k=\frac{1}{F_1/\sigma_{k,1}+(1-F_1)/\sigma_{k,2}},\sigma_\omega=\frac{1}{F_1/\sigma_{\omega,1}+(1-F_1)/\sigma_{\omega,2}},F_1=\tanh\left(\phi_1^4\right),\phi_1=\min\left[\max\left(\frac{\sqrt{k}}{0.09\omega y},\frac{500\mu}{\rho y^2\omega}\right),\frac{4\rho k}{\sigma_{\omega,2}D_\omega^+y^2}\right]$$

$$F_2=\tanh\left(\phi_2^4\right),\phi_2=\max\left(\frac{2\sqrt{k}}{0.09\omega y},\frac{500\mu}{\rho y^2\omega}\right),D_\omega^+=\max\left[2\rho\frac{1}{\sigma_{\omega,2}}\frac{1}{\omega}\frac{\partial k}{\partial x_j}\frac{\partial \omega}{\partial x_j},10^{-20}\right],\alpha_\infty=F_1\alpha_{\infty,1}+(1-F_1)\alpha_{\infty,2},\alpha_{\infty,1}=\frac{\beta_{i,1}}{\beta_\infty{}^*}-\frac{\kappa^2}{\sigma_{\omega,1}\sqrt{\beta_\infty{}^*}},\alpha_{\infty,2}=\frac{\beta_{i,2}}{\beta_\infty{}^*}\frac{\kappa^2}{\sigma_{\omega,2}\sqrt{\beta_\infty{}^*}}$$

$$\beta_i=F_1\beta_{i,1}+(1-F_1)\beta_{i,2},\beta^*,\beta,\alpha^*,\beta_{i,1},\beta_{i,2},\sigma_{k,1},\sigma_{\omega,1},\sigma_{k,2},\sigma_{\omega,2},a_1,\alpha_\infty{}^*,\alpha_0,\beta_\infty{}^*,R_\beta,R_k,R_\omega,\varsigma^*,M_{t0},\kappa \qquad \text{(Model parameters)}$$

REFERENCES

[1] Chang TJ, Hsieh YF, Kao HM. Numerical investigation of airflow pattern and particulate matter transport in naturally ventilated multi-room buildings. Indoor Air 16. 2006. http://dx.doi.org/10.1111/j.1600-0668.2005.00410.x

[2] Li X, Inthavong K, Ge Q, Tu J. Numerical investigation of particle transport and inhalation using standing thermal manikins. Building Environ. 2013; 60: 116-125. http://dx.doi.org/10.1016/j.buildenv.2012.11.014

[3] Li X, Inthavong K, Tu J. Numerical investigation of micron particle inhalation by standing thermal manikins in horizontal airflows. Indoor and Built Environment: 2014; 1420326X14551069.

[4] Nielson PV. Flow in air conditioned rooms, Technical University of Denmark, Copenhagen, Denmark. 1974.

[5] Luo S, Heikkinen J, Roux B. Simulation of air flow in the IEA Annex 20 test room—validation of a simplified model for the nozzle diffuser in isothermal test cases. Building Environ. 2004; 39:1403-1415. http://dx.doi.org/10.1016/j.buildenv.2004.04.006

[6] Zhai Z. Application of Computational Fluid Dynamics in Building Design: Aspects and Trends. Indoor Built Environ. 2006; 15: 305-313. http://dx.doi.org/10.1177/1420326X06067336

[7] Nielsen PV, Awbi HB, Davidson L, Schalin A. Computational Fluid Dynamics in Ventilation Design, REHVA Guidebook No. 10. Federation of Europian Heating and Air-conditioning Associations, REHVA, ISBN. 2007; 2-9600468-9-7.

[8] Chen Q. Computational fluid dynamics for HVAC - successes and failures. ASHRAE Transactions, 1997; 103: 178-187.

[9] AIAA. Guide for the verification and validation of computational fluid dynamics simulations, in AIAA G-077-1998, Reston, VA.

[10] Stern F, Wilson R, Shao J. Quantitative V&V of CFD simulations and certification of CFD codes. Int J Numer Meth Fluids, 2006; 50:1335-1355. http://dx.doi.org/10.1002/fld.1090

[11] Sorensen DN, Nielsen PV. Quality control of computational fluid dynamics in indoor environments. Indoor Air, 2003; 13: 2-17. http://dx.doi.org/10.1111/j.1600-0668.2003.00170.x

[12] Chung KC. Three-dimensional analysis of airflow and contaminant particle transport in a partitioned enclosure. Building Environ. 1999; 34: 7-17. http://dx.doi.org/10.1016/S0360-1323(97)00073-5

[13] Abanto J, Barrero D, Reggio M, Ozell BT. Airflow modelling in a computer room. Building Environ. 2004; 39: 1393-1402. http://dx.doi.org/10.1016/j.buildenv.2004.03.011

[14] Cheong KWD, Djunaedy E, Poh TK, Tham KW, Sekhar SC, Wong NH, *et al*. Measurements and computations of contaminant's distribution in an office environment. Building Environ 2003; 38: 135-145. http://dx.doi.org/10.1016/S0360-1323(02)00031-8

[15] Ge Q, Li X, Inthavong K, Tu J. Numerical study of the effects of human body heat on particle transport and inhalation in indoor environment. Building Environ 2013; 59: 1-9. http://dx.doi.org/10.1016/j.buildenv.2012.08.002

[16] Inthavong K, Ge QJ, Li A, Tu JY. Source and trajectories of inhaled particles from a surrounding environment and its deposition in the respiratory airway. Inhalation Toxicol 2013; 25: 280-291. http://dx.doi.org/10.3109/08958378.2013.781250

[17] King Se CM, Inthavong K, Tu J. Inhalability of micron particles through the nose and mouth. Inhalation Toxicol 2010; 22: 287-300. http://dx.doi.org/10.3109/08958370903295204

[18] Chen Q. Comparison of different k-ε models for indoor airflow computations. Numerical Heat Transfer, Part B: Fundamentals 1995; 28: 353-369. http://dx.doi.org/10.1080/10407799508928838

[19] Rouaud O, Havet M. Computation of the airflow in a pilot scale clean room using K-ε turbulence models. Int J Refrigeration 2002; 25: 351-361. http://dx.doi.org/10.1016/S0140-7007(01)00014-7

[20] Gebremedhin KG, Wu BX. Characterization of flow field in a ventilated space and simulation of heat exchange between cows and their environment. J Thermal Biol 2003; 28: 301-319. http://dx.doi.org/10.1016/S0306-4565(03)00007-X

[21] Nielsen PV. Specification of a Two-Dimensional Test Case, Aalborg University, IEA Annex 20: Air Flow Patterns within Buildings 1990.

[22] Sørensen DN, Nielsen PV. Quality control of computational fluid dynamics in indoor environments. Indoor Air 2003; 13: 2-17. http://dx.doi.org/10.1111/j.1600-0668.2003.00170.x

[23] Voigt LK. Validation of Turbulence Models using Topological Aspects, in ROOMVENT 2002; 173-176.

[24] Demuren AO, Rodi W. Calculation of turbulence-driven secondary motion in non-circular ducts. J Fluid Mech 1984; 140: 189-222. http://dx.doi.org/10.1017/S0022112084000574

[25] Heschl C, Inthavong K, Sanz W, Tu J. Evaluation and improvements of RANS turbulence models for linear diffuser flows. Comput Fluids 2013; 71: 272-282. http://dx.doi.org/10.1016/j.compfluid.2012.10.015

[26] van Hooff T, Blocken B, van Heijst GJF. On the suitability of steady RANS CFD for forced mixing ventilation at transitional slot Reynolds numbers. Indoor Air 2012; n/a-n/a.

[27] Heschl C, Inthavong K, Sanz W, Tu J. Nonlinear eddy viscosity modeling and experimental study of jet spreading rates. Indoor Air 2014; 24: 93-102. http://dx.doi.org/10.1111/ina.12050

[28] Nielsen PV. The selection of turbulence models for prediction of room airflow. ASHRAE Transactions 1998; 104: 1119-1127.

[29] Zhang Z, Zhang W, Zhai Z, Chen Q. Evaluation of various turbulence models in predicting airflow and turbulence in enclosed environments by CFD: part-2: Comparison with experimental data from literature. HVAC&R Res 2007; 13: 871-886. http://dx.doi.org/10.1080/10789669.2007.10391460

[30] Ito K, Kato S, Murakami S. Model experiment of flow and temperature field in room for validating numerical simulation analysis of newly proposed ventilation effectiveness. J Architect Planning Environ Eng 2000; 534: 49-56.

[31] Lemaire AD, Chen Q, Ewert M, Heikkinen J, Inard C, Moser A, *et al*. Room air and contaminant flow, evaluation of computational methods. Subtask-1 Summary Report, in International Energy Agency, Annex 20, TNO Building and Construction Research, Delft 1993. The Netherlands.

[32] Chen Q, Glicksman LR. Application of computational fluid dynamics for indoor air quality studies,. McGraw-Hill, Inc. 2000.

[33] Launder BE, Spalding DB. The numerical computation of turbulent flows. Comput Meth Appl Mech Eng 1974; 3: 269-289. http://dx.doi.org/10.1016/0045-7825(74)90029-2

[34] Abe K, Kondoh T, Nagano Y. A new turbulence model for predicting fluid flow and heat transfer in separating and reattaching flows—II. Thermal field calculations. Int J Heat Mass Transfer 1995; 38: 1467-1481. http://dx.doi.org/10.1016/0017-9310(94)00252-Q

[35] Yakhot V, Orszag SA. Renormalization group analysis of turbulence. I. Basic theory. J Sci Comput 1986; 1: 3-51. http://dx.doi.org/10.1007/BF01061452

[36] Wilcox D. Turbulence Modeling for CFD. DCW Industries, Inc., 5354 Palm Drive, La Canada, California 91011. 1993.

[37] Menter FR, Kuntz M, Langtry RB. Ten Years of Industrial Experience with the SST Turbulence Model, in Turbulence, Heat and Mass Transfer 4, K. Hanjalic, Y. Nagano, M. Tummers, eds, Begell House Inc 2003; 625-632.

[38] Murakami S, Kato S, Nakagawa H. Numerical and experimental study for flow and temperature fields in rooms with horisontal nonisothermal jets. J Architect Planning, Environ Eng 1991; 423: 11-21.

[39] Kato S, Murakami S, Kondo T. Numerical study of nonisothermal three-dimensional room airflow: Room airflow analysis by means of algebraic stress model Part 4. J Architect Planning, Environ Eng 1993; 443: 15-20.

[40] Ooka R, Murakami S, Kato S. Numerical Simulation of Room Airflow by Means of Differential Stress Model part 2: 3-D Simulation for Buoyant Flow comparing with ASM results. Summaries of Technical Papers of Committee Meeting Architectural Institute of Japan 1992; 519-520.

[41] Mizutani K, Murakami S, Mochida A, Tominaga T. Large Eddy Simulation of Non-Isothermal Room Airflow. Summaries of Technical Papers of Committee Meeting Architectural Institute of Japan 1992; 625-628.

Received on 01-12-2014 Accepted on 18-12-2014 Published on 07-04-2015

DOI: http://dx.doi.org/10.15377/2409-9821.2015.02.01.1